

## Hadronic Scenario for Galactic PeVatron LHAASO J1912+1014u Supported by *Fermi*-LAT $\gamma$ -ray Data and FUGIN CO Data

TSUNEFUMI MIZUNO,<sup>1</sup> HIDETOSHI SANO,<sup>2</sup> TAKERU MURASE,<sup>2</sup> TOMOHIKO OKA,<sup>3</sup> HIROMASA SUZUKI,<sup>4</sup> AND NAOHITO NAKAHARA<sup>1</sup>

<sup>1</sup>*Hiroshima University*

<sup>2</sup>*Gifu University*

<sup>3</sup>*Institute for Theoretical Physics and Astrophysics, Julius-Maximilians-Universität Würzburg, Emil-Fischer-Str. 31, 97074 Würzburg, Germany*

<sup>4</sup>*Miyazaki University*

### ABSTRACT

LHAASO has reported 43 sub-PeV  $\gamma$ -ray sources, which are promising candidates for cosmic-ray (CR) accelerators above the PeV energy, commonly called as PeVatrons. Multi-wavelength observations are crucial for identifying the underlying particle species and estimating the CR energy content of these sources. In this work we investigate the region around LHAASO J1912+1014u (and HESS J1912+101) using *Fermi*-LAT  $\gamma$ -ray data and FUGIN CO data. We analyzed 15 years of *Fermi*-LAT data in the 0.4–409.6 GeV energy range. By improving the standard *Fermi*-LAT diffuse emission model, we significantly reduced the large residuals around the source in the 1.6–12.8 GeV band. We detected a statistically significant excess above the diffuse background, which likely represents  $\geq 10$  GeV emission associated with the LHAASO/H.E.S.S. source. The GeV excess exhibits a hard spectrum (photon index of about 2.1) and is well reproduced by interstellar gas templates with systemic velocities of about 25 km s<sup>-1</sup> or 60 km s<sup>-1</sup>. We performed a comprehensive fit to the GeV–TeV spectral energy distribution. Although a leptonic scenario can reproduce the observed spectrum, a hadronic scenario is favored once electron cooling is considered. The inferred CR proton spectrum has an index of  $\sim 2.2$ , and the total CR proton energy above 1 GeV is  $(1\text{--}5) \times 10^{49}$  erg, depending on the assumed velocity range of the associated interstellar gas. A stringent upper limit on diffuse X-ray emission further supports the proton PeVatron scenario.

*Keywords:* Galactic cosmic rays (567) — Cosmic ray sources (328) — Gamma-ray sources (633) — Diffuse molecular clouds (381) — Interstellar atomic gas (833) —

### 1. INTRODUCTION

Cosmic-ray (CR) hadrons below the knee energy ( $\sim 3 \times 10^{15}$  eV) are believed to be produced and confined in the Milky Way Galaxy. Hadronic CRs with energies of petaelectronvolts (PeV) should have gained energies at powerful particle accelerators in our Galaxy, and identifying such accelerators called “PeVatrons” is of significant interest in modern astrophysics. A PeVatron will produce intense  $\gamma$ -ray emission above 100 TeV through nucleon–nucleon interactions at the nearby interstellar medium (ISM) clouds. The Tibet AS  $\gamma$  experiment, a high-altitude CR and  $\gamma$ -ray observatory located in Tibet, discovered a sub-PeV  $\gamma$ -ray source that is positionally coincident with the molecular clouds toward the supernova remnant (SNR) G106.3+2.7 (Tibet AS $\gamma$  Collaboration et al. 2021). Subsequently, the Large High Altitude Air Shower Observatory (LHAASO, X.-H. Ma et al. 2022) reported more than 40 sub-PeV sources in its first source catalog (Z. Cao et al. 2024).

One caveat is that while CR hadrons primarily produce sub-PeV  $\gamma$ -rays via nucleon–nucleon interactions, CR electrons and positrons (leptons) can also contribute to the sub-PeV  $\gamma$ -rays flux through inverse-Compton (IC) scattering off ambient soft photons. Indeed, the Crab Nebula, a bright pulsar wind nebula (PWN) and an established CR electron/positron accelerator, is one of the LHAASO sub-PeV sources. The spatial distribution of  $\gamma$ -ray emission is

key to distinguishing proton PeVatrons from electron PeVatrons, but the moderate angular resolution of LHAASO ( $0^\circ.3\text{--}0^\circ.8$  in 10–100 TeV; X.-H. Ma et al. 2022) prevents us from making a firm identification in most cases. Although atmospheric Cherenkov detectors have excellent angular resolution ( $\sim 0^\circ.08$ ; e.g., H. E. S. S. Collaboration et al. 2018a), their small field of view often prevents the firm identification of LHAASO sub-PeV sources, which typically have angular extents  $\geq 0^\circ.5$ .

With these scientific motivations and technical considerations in mind, we searched for a GeV counterpart of the sub-PeV source LHAASO J1912+1014u using the *Fermi* Large Area Telescope (LAT; W. B. Atwood et al. 2009). The *Fermi*-LAT, with its wide field-of-view ( $\sim 2.4$  sr), good angular resolution ( $\sim 0^\circ.1$  above 10 GeV; see official *Fermi*-LAT Performance webpage<sup>5</sup>), and substantial photon statistics (more than 17 years of operation), is suitable for our study. The source was found to be extended (39% radii when modeled by a 2D Gaussian,  $r_{39}$ , are  $0^\circ.36$  and  $0^\circ.50$  in the WCDA band (1–25 TeV) and the KM2A band ( $\geq 25$  TeV) of LHAASO, respectively) and was significantly detected above 100 TeV at  $\geq 8\sigma$ . There is an old, powerful pulsar PSR J1913+1011 (D. J. Morris et al. 2002) inside the WCDA/KM2A Gaussians, and another sub-PeV source LHAASO J1914+1150u about  $1^\circ.4$  away. Our source of interest (LHAASO J1912+1014u)

is positionally coincident (source separation of only  $\sim 0^\circ.1$ ) with the well-known TeV source HESS J1912+101 (F. Aharonian et al. 2008a; H. E. S. S. Collaboration et al. 2018b), which exhibits a shell-like morphology. Considering a small angular separation and comparable source sizes, we will assume that LHAASO J1912+1014u and HESS J1912+101 are the same object and call them collectively the “LHAASO/H.E.S.S. source” whenever we describe both sources. Although several studies have been done on HESS J1912+101 in the GeV energy band (Y. Li et al. 2023; X.-N. Sun et al. 2022; H. Zeng et al. 2021; H.-M. Zhang et al. 2020), the nature of the source has not been settled yet. This is mainly due to the difficulty in modeling the background diffuse emission and the source spatial distribution.

In this new study of the HESS J1912+101 (and LHAASO J1912+1014u) region, we constructed a custom background model. We revealed an extended  $\gamma$ -ray excess over known sources and Galactic diffuse emission above 10 GeV, coincident in position with the LHAASO sub-PeV source. To accurately trace the ISM gas toward the object, we prepared two  $W_{\text{CO}}$  maps (maps of the integrated  $^{12}\text{CO}$  (J=1–0) 2.6-mm line intensity) using high-resolution FUGIN CO data (T. Umemoto et al. 2017). We also included the contribution of atomic gas around the molecular clouds. We then used those ISM gas templates and fit the *Fermi*-LAT data to characterize the spectrum and morphology of the extended emission in the GeV energy band. This paper is organized as follows: in Section 2, we describe  $\gamma$ -ray observations and data selection, and the preparation of the ISM gas templates. In Section 3, we present the results of the data analysis, which confirm that our ISM gas maps reproduce the  $\gamma$ -ray excess as well as, or better than, simple Gaussian models. In Section 4, we discuss possible scenarios based on the spectral and spatial distributions of  $\gamma$  rays measured by *Fermi*-LAT in combination with the published multiwavelength data. Finally, in Section 5, we present a summary of the study and prospects.

## 2. OBSERVATIONS

### 2.1. Gamma-ray Observation, Data Selection, and Analysis Procedure

*Fermi*-LAT is a pair-tracking  $\gamma$ -ray telescope that detects photons from  $\sim 20$  MeV to more than 300 GeV. Thanks to its wide field of view ( $\sim 2.4$  sr) and good angular resolution ( $\sim 0^\circ.1$  above 10 GeV), *Fermi*-LAT is an ideal telescope for searching for the counterpart of extended TeV  $\gamma$ -ray sources in the Milky Way. Routine science operations with the LAT started on August 4, 2008. We have accumulated events from August 4, 2008, to August 2, 2023 (i.e., 15 years) to study GeV properties of the LHAASO/H.E.S.S. source. We used the standard LAT analysis software, *Fermitools*<sup>6</sup> v2.2.0. We also employed an analysis pipeline, *Fermipy*<sup>7</sup> v1.3.1, a Python package based on *Fermitools* that enables automated analyses (M. Wood et al. 2017).

We defined our region of interest (ROI) of  $15^\circ \times 15^\circ$  in Galactic coordinates centered at the position of LHAASO J1912+1014u in the KM2A band (Galactic longitude  $l$  and latitude  $b$  to be  $(l, b) = (44^\circ.78, -0^\circ.06)$ ), and selected all PSF type events of the SOURCE class. We required that the reconstructed zenith angles of the arrival directions of the photons be less than  $100^\circ$  to reduce contamination by photons from Earth’s atmosphere. We used the data from 0.4 to 409.6 GeV and binned them with pixel sizes of  $0^\circ.25$ ,  $0^\circ.1$ , and  $0^\circ.05$  in the 0.4–1.6 GeV, 1.6–12.8 GeV,

<sup>5</sup> [https://www.slac.stanford.edu/exp/glast/groups/canda/lat\\_Performance.htm](https://www.slac.stanford.edu/exp/glast/groups/canda/lat_Performance.htm)

<sup>6</sup> <https://fermi.gsfc.nasa.gov/ssc/data/analysis/software/>

<sup>7</sup> <https://fermipy.readthedocs.io/en/latest/>

and above 12.8 GeV ranges, respectively. This procedure aims to fully utilize the angular resolution of the *Fermi*-LAT while keeping the fitting computation cost reasonable.

To analyze the source spectrum and morphology, we applied binned maximum likelihood to the ROI. We employed the latest response functions, P8R3\_SOURCE\_V3 (W. Atwood et al. 2013; P. Bruel et al. 2018). We used a standard diffuse background model (gll\_iem\_v07.fits<sup>8</sup>), an isotropic spectral template (iso\_P8R3\_SOURCE\_V3\_v1.txt), and point source models from the fourth *Fermi*-LAT catalog (4FGL-DR4) as described by S. Abdollahi et al. (2022) and J. Ballet et al. (2023). Additionally, we developed a customized background model as detailed in Section 3.1. We let the normalizations of 4FGL sources within  $7^\circ.5$  of the ROI's center free to vary, and the normalizations and spectral indices of the sources within  $2^\circ.0$  free to vary. We also allowed the Galactic diffuse background model (normalization and index) and isotropic spectral template (normalization) to vary freely. In testing several templates for the GeV counterpart of the LHAASO/H.E.S.S. source, we evaluated the test statistic (TS) defined as  $TS = 2(\ln L_1 - \ln L_0)$ , where  $L_1$  and  $L_0$  are the maximum likelihood values with and without the source template. The value of TS follows the  $\chi^2$  distribution of the degree of freedom to be the number of free parameters (J. R. Mattox et al. 1996). When we compare models of the different number of free parameters, we also used the Akaike Information Criterion (AIC) defined with the same sign as TS.

## 2.2. HI and CO Observations and Target Gas Templates

Galactic proton PeVatrons will produce hard  $\gamma$ -ray emission in the GeV and TeV energy ranges through the interaction with nearby ISM clouds. Dense clouds are primarily in the molecular phase (molecular clouds) and are conventionally traced indirectly via carbon monoxide (CO) line emission (e.g., T. M. Dame et al. 2001). CO line observations enable us to decompose molecular clouds along the line of sight and estimate the distance to the source.

F. Aharonian et al. (2008a) reported a possible association of HESS J1912+101 with CO-line emission in the systemic velocity ( $V_{\text{LSR}}$ ) ranging 50–70 km s<sup>-1</sup>. Later, Y. Su et al. (2017) claimed that molecular clouds with  $V_{\text{LSR}} \sim 60$  km s<sup>-1</sup>, together with shocked molecular gas and high-velocity atomic shells, are concentrated toward the shell-like TeV source. Subsequent studies of HESS J1912+101 (e.g., X.-N. Sun et al. 2022; Y. Li et al. 2023) used CO maps of this velocity range. H. Sano et al. (2018), on the other hand, pointed out that the high velocity of the clouds identified by Y. Su et al. (2017) could be due to an H II region along the line of sight, and proposed an alternative velocity of  $V_{\text{LSR}} \sim 25$  km s<sup>-1</sup>. The clouds of this velocity range also exhibit a shell-like structure in the CO distribution, which coincides with HESS J1912+101 (H. Sano et al. in preparation). To discuss the association of these ISM structures with the LHAASO/H.E.S.S. source, we used <sup>12</sup>CO data from the high-resolution FUGIN CO survey (T. Umemoto et al. 2017). The effective angular resolution is  $\sim 20''$ . Because an artificial striped pattern along the scanning direction was identified in the publicly available FUGIN data, we reprocessed the data using the NOSTAR software package provided by the Nobeyama Radio Observatory (see Section 5.1 in T. Sawada et al. 2008). Details of the reprocessing are described in T. Murase et al. (2026). We used  $W_{\text{CO}}$  maps of <sup>12</sup>CO in the velocity ranges 58.3–62.2 km s<sup>-1</sup> and 23.2–26.4 km s<sup>-1</sup> to model CO clouds proposed by Y. Su et al. (2017) and H. Sano et al. (2018), respectively. We adopted a nominal value for  $X_{\text{CO}}$  ( $2.0 \times 10^{20}$  cm<sup>-2</sup>(K km s<sup>-1</sup>)<sup>-1</sup>; e.g., D. L. Bertsch et al. 1993) to convert  $W_{\text{CO}}$  to an H<sub>2</sub> column density, yielding the proton column density of molecular gas as  $N_{\text{p}}(\text{H}_2) = 2 \cdot X_{\text{CO}} \cdot W_{\text{CO}}$ .

Through detailed correlation among ISM gas tracers in high-latitude regions, a considerable amount of gas, likely cold and optically thick HI, was revealed around the molecular clouds traced by CO line emission (e.g., Y. Fukui et al. 2015; T. Mizuno et al. 2025). The proton column density of atomic gas,  $N_{\text{p}}(\text{HI})$ , is usually derived under the assumption that the 21 cm HI line is optically thin; however, if optically thick HI is present, the column density will be underestimated by up to a factor of about two (Y. Fukui et al. 2014; Y. Fukui et al. 2015). In this study, we derived the corrected  $N_{\text{p}}(\text{HI})$  map using the empirical correlation between  $W_{\text{HI}}$  (the integrated 21 cm HI line intensity) and the dust optical depth as derived by Y. Fukui et al. (2017). The velocity integration ranges of  $W_{\text{HI}}$  are identical to those for the CO data. We used the HI data from the VLA Galactic Plane Survey (VGPS; J. M. Stil et al. 2006), which has a spatial resolution (full width at half maximum) of  $\sim 60''$ .

From the  $N_{\text{p}}(\text{HI})$  map including the contribution of optically-thick HI, and the  $N_{\text{p}}(\text{H}_2)$  map as described above, we constructed proton column density ( $N_{\text{p}}$ ) maps for the Su et al. (2017) velocity range and the Sano et al. (2018) velocity range. We smoothed the <sup>12</sup>CO data to match the HI data resolution before adding the  $N_{\text{p}}(\text{HI})$  and  $N_{\text{p}}(\text{H}_2)$

<sup>8</sup> <https://fermi.gsfc.nasa.gov/ssc/data/access/lat/BackgroundModels.html>

maps. We will use the obtained  $N_p$  maps in the  $\gamma$ -ray data analysis in Section 3.

### 3. DATA ANALYSIS AND RESULTS

#### 3.1. Baseline Model

Our first step was to establish a baseline model to identify the GeV counterpart of the LHAASO/H.E.S.S. source. We fit the data using a standard diffuse model, isotropic template, and 4FGL sources. The results showed significant, extended residuals next to the LHAASO/H.E.S.S. source (toward positive Galactic longitude) in the 1.6–12.8 GeV range, as shown in Figure 1(a). We also observed a striped residual above 12.8 GeV in areas connecting  $(l, b) \sim (46^\circ 0, 0^\circ 0)$  to  $(45^\circ 5, -0^\circ 5)$ , as shown in Figure 1(b). The substantial size of the residuals below 12.8 GeV indicates that they are not due to unmodeled point sources, but rather to the inadequate modeling of the ISM gas. The standard diffuse model was constructed from atomic gas templates (traced by the 21 cm H I line), molecular gas templates (traced by the CO 2.6 mm line), and a dark neutral medium (DNM) template (constructed from dust emission that is not well correlated with H I and CO lines). The model uses a single DNM template because dust emission contains no velocity information, and residuals will appear unless the ratio of  $\gamma$ -ray intensity to the estimated DNM column density in the ROI agrees well with that of the all-sky average. We observed significant residuals where the DNM template intensity is high, as shown in Figure 1(c), indicating an underestimation of the DNM in this area. To address this, we included the DNM template in our model as an additional ISM gas template. The spectrum for the additional DNM template is soft and follows a power law with a photon index of  $\sim 2.7$  above 2 GeV, supporting it as unmodeled ISM gas. The striped residual above 12.8 GeV remains and is likely associated with another sub-PeV source, LHAASO J1914+1150u, rather than our target, LHAASO J1912+1014u. We employed three point sources to model this residual phenomenologically (see Figure 1(b) for their positions). They showed hard spectra (best-fit indices of 1.6–2.2), and we fixed their indices to 2.0 for simplicity.

These additions, which we refer to as the “baseline model”, significantly reduced the residuals as shown in Figures 1(d) and (e). However, largely extended and structured excess emission above 12.8 GeV remains in areas toward the LHAASO/H.E.S.S. source, as indicated in Figure 1(e). We interpret this as the GeV counterpart of the LHAASO/H.E.S.S. source and will examine its spatial and spectral properties in the following sections.

We remind that there are two catalog sources marked with an identifier of “c” (coincident with interstellar clumps) within the LHAASO  $r_{39}$  radii of WCDA and KM2A Gaussian, namely 4FGL J1911.7+1014c and 4FGL J1914.7+1012c (see Figure 1 for their locations). They were not included to model the background in some of the past studies of *Fermi*-LAT data on HESS J1912+101 (e.g., H. Zeng et al. 2021; X.-N. Sun et al. 2022; Y. Li et al. 2023). We found that their spectra are soft, similar to that of the additional DNM template. We interpret this as indicating that these sources are not the GeV counterparts of the LHAASO/H.E.S.S. source, but rather arise from another unmodeled (clumpy) ISM gas component. Accordingly, we continue to include them (and all other sources with a “c” identifier in our ROI) as point sources in the following analysis.

#### 3.2. Modeling the GeV Counterpart of the LHAASO/H.E.S.S. Source

We observed an extended hard excess (diameter greater than  $1^\circ$ ), likely the GeV counterpart of the LHAASO/H.E.S.S. source. As a preliminary analysis, we evaluated its size using a uniform-disk model. The position and radius of it (determined using `extension` method in `Fermipy`) are  $(l, b) = (44^\circ 56 \pm 0^\circ 08, -0^\circ 05 \pm 0^\circ 08)$  and  $0^\circ 86 \pm 0^\circ 04$ , respectively. Modeling the excess with this uniform disk and a power-law spectrum yields a TS value of  $\sim 100$  and a hard spectrum with the photon index of  $\sim 2.1$ , as reported in Table 1. Accordingly, we detected a largely extended (radius  $\geq 0^\circ 8$ ) GeV excess. The observed hard spectrum demonstrates that this excess originates from a CR accelerator rather than from unmodeled gas. To investigate the physical origin of this excess, we tested five templates prepared a priori, each chosen for its potential to accurately represent the excess emission: the H.E.S.S. intensity map,  $N_p$  maps of  $V_{\text{LSR}}$  in 58.3–62.2 km s $^{-1}$  (Y. Su et al. 2017) and  $V_{\text{LSR}}$  in 23.2–26.4 km s $^{-1}$  (H. Sano et al. 2018), and two Gaussian models of LHAASO J1912+1014u in Z. Cao et al. (2024). The H.E.S.S. intensity map was constructed from the H.E.S.S. Galactic plane survey (H. E. S. S. Collaboration et al. 2018a) and is publicly available<sup>9</sup>. This map will provide a template for the counterpart of HESS J1912+101. Two  $N_p$  maps were constructed from H I and CO data (Section 2.2). They will be used to model the distribution of the target gas, either for protons (via

<sup>9</sup> <https://www.mpi-hd.mpg.de/HESS/hgps/>

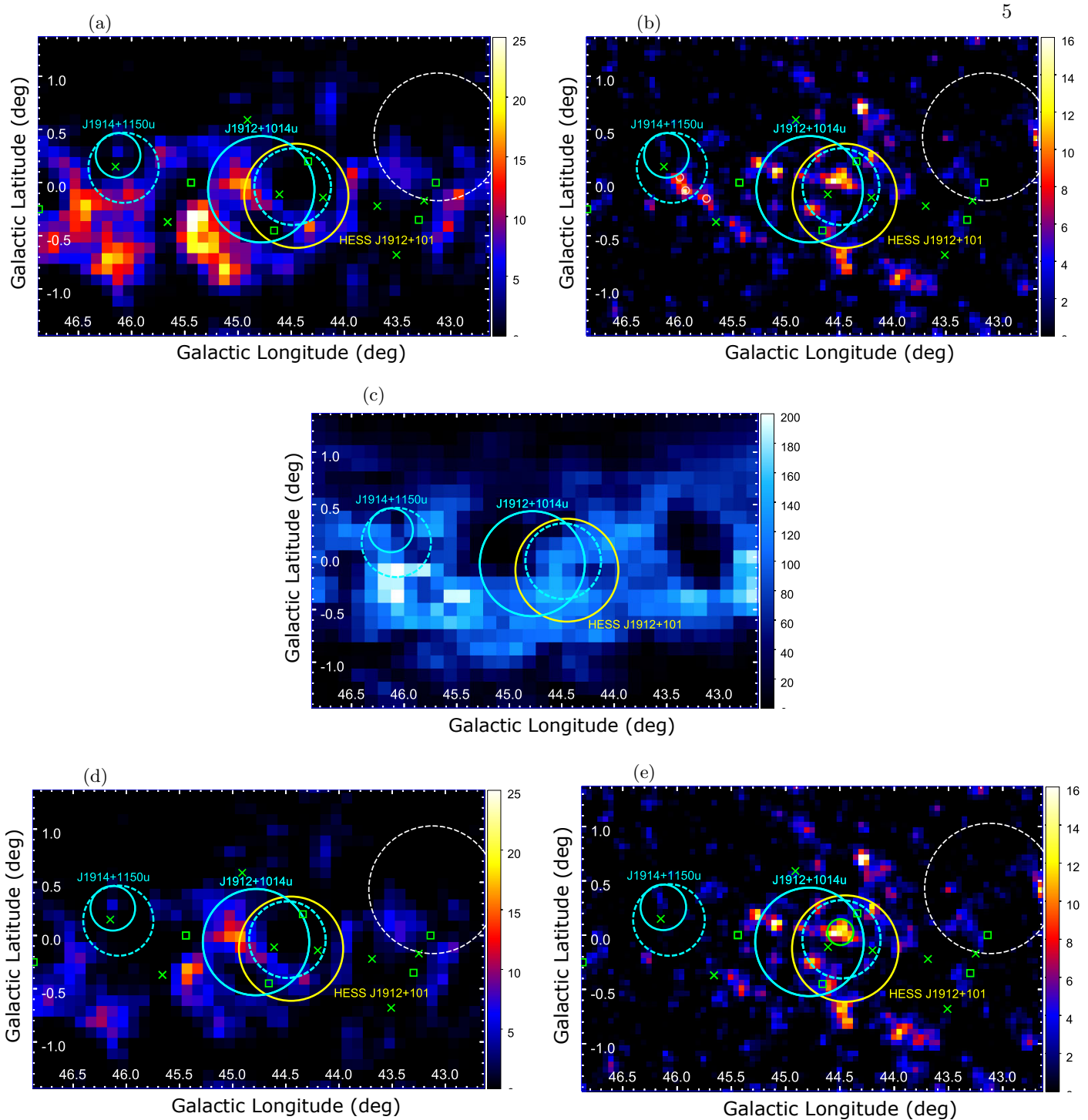


**Figure 1.** (a) The TS map in 1.6–12.8 GeV constructed using standard background models. The 4FGL sources are marked by squares (for those with a “c” identifier) and crosses (for others). The position and size of 4FGL J1908.6+0915e, modeled by a uniform disk, are shown by a white dashed circle. LHAASO sub-PeV sources, modeled by a 2D Gaussian, are indicated by cyan dashed (WCDA) and solid (KM2A) circles. The position and size of HESS J1912+101, modeled by a spherical shell in H. E. S. S. Collaboration et al. (2018b), are shown by a yellow circle. (b) The same as panel (a), but in  $\geq 12.8$  GeV instead of 1.6–12.8 GeV. Three point sources to model the striped residual near LHAASO J1914+1150u are indicated by small pink circles. (c) The DNM template map (in arbitrary units) used to construct the standard diffuse model, which is internally available to the *Fermi*-LAT collaboration. (d) The same as panel (a), but when modeled with the additional ISM gas template and three point sources. (e) The same as panel (b), but when modeled with the additional ISM gas template and three point sources. A green circle at  $(l, b) \sim (44.5, 0.0)$  indicates the small peak-like structure studied in Section 4.4.

hadronic interactions) or electrons (via electron Bremsstrahlung). Two Gaussians are phenomenological models aimed to represent the GeV counterpart of LHAASO J1912+1014u. The H.E.S.S. intensity map, the  $N_p$  map of Su et al. (2017) velocity range, and the  $N_p$  map of Sano et al. (2018) velocity range, are shown in Figures 2(a)–(c).

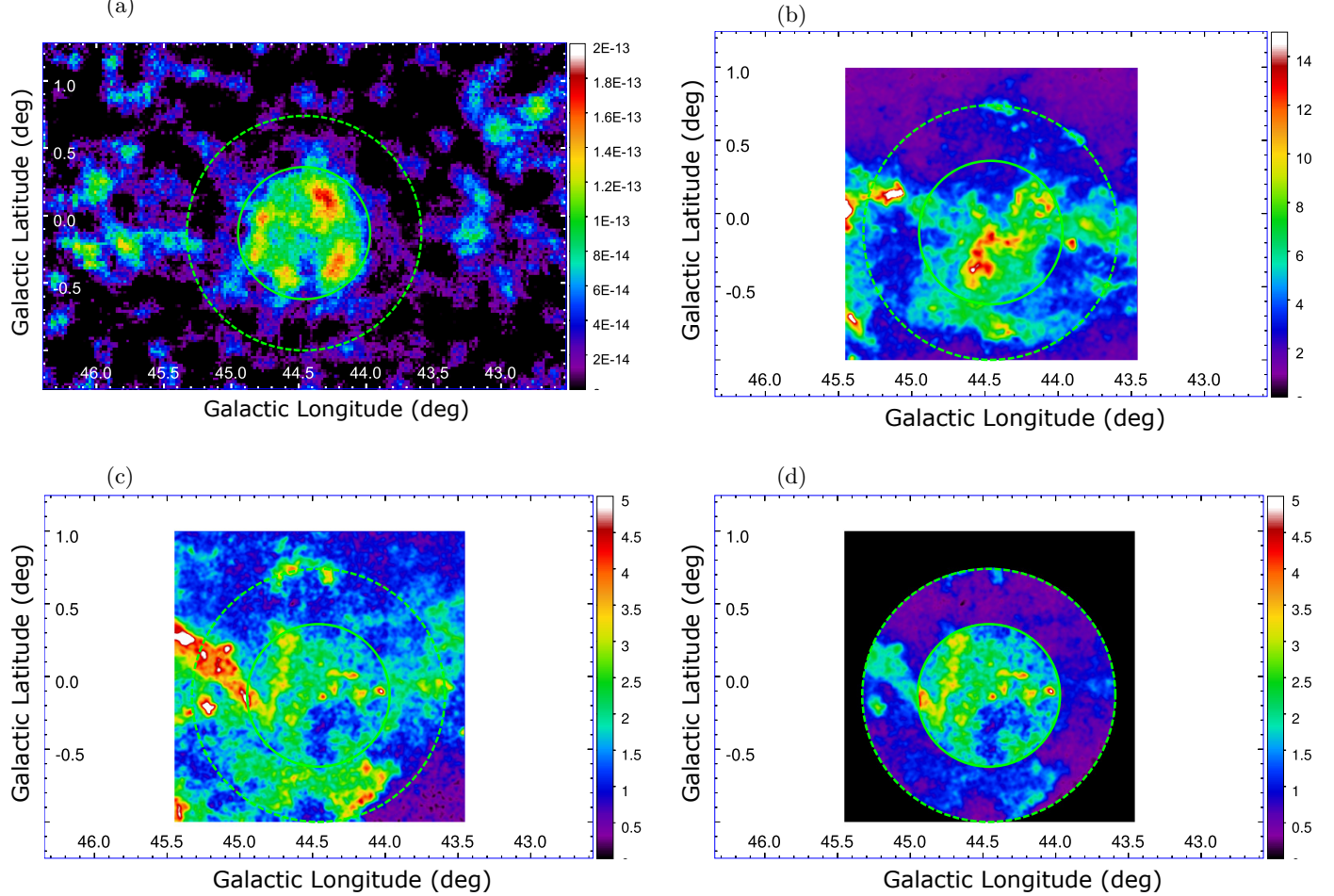


**Figure 2.** Template maps tested to reproduce the GeV excess emission toward the LHAASO/H.E.S.S. source. (a) The H.E.S.S. intensity map. (b) The  $N_p$  map of Su et al. (2017) velocity range ( $58.4\text{--}62.2\text{ km s}^{-1}$ ). (c) The  $N_p$  map of Sano et al. (2018) velocity range ( $23.2\text{--}26.4\text{ km s}^{-1}$ ). (d) The same as (c), but  $N_p$  in the annulus is scaled by  $1/2.10$  (see text for details). There, the solid circle (radius of  $0^\circ.49$ ; the same as the yellow circle in Figure 1) shows the size of the spherical shell of HESS J1912+101 used in the initial modeling, and the dashed circle (radius of  $0^\circ.87$ ) shows the area used in the final modeling. The H.E.S.S. intensity map is arbitrarily scaled to be compatible with Fermitools. The unit of  $N_p$  maps is  $10^{21}\text{ cm}^{-2}$ .

We first examined the excess emission in the HESS J1912+101 region using the H.E.S.S. intensity map and two  $N_p$  maps. To compare the three templates in a self-consistent manner and to compare our results with previous works (e.g., H.-M. Zhang et al. 2020; X.-N. Sun et al. 2022; Y. Li et al. 2023), we selected a circle of  $0^\circ.49$  radius centered at  $(l, b) = (44^\circ.46, -0^\circ.13)$ . This area is determined to match the outer boundary of the spherical shell used to model HESS J1912+101 in H. E. S. S. Collaboration et al. (2018b). We modeled each template with a power-law spectrum. The TS values were 60.0, 60.8, and 68.6 for the H.E.S.S. intensity map, the Su et al. (2017)  $N_p$  map, and the Sano et al. (2018)  $N_p$  map, respectively, with similar photon indices ( $\sim 2.05$ ). Accordingly, all three templates significantly improve the fit (by more than  $7\sigma$ ). We also found that without sources with a “c” identifier in the background model, the fit worsens (by about 20 in  $\ln L$ ) and the spectrum softens below 10 GeV. We understand that this is why most pioneering work on *Fermi*-LAT data to search for the HESS J1912+101 counterpart (e.g., H. Zeng et al. 2021; X.-N. Sun et al. 2022; Y. Li et al. 2023) reported soft spectra below 10 GeV.

Next, we examined the entire area of the observed excess emission (diameter greater than  $1^\circ$ ). To do this, we employed the same three maps but with a radius of  $0^\circ.87$ . This radius was chosen not to exceed the boundary of FUGIN CO maps and match the size of the uniform-disk model in the initial analysis. We also used two LHAASO

Gaussians (one with  $r_{39} = 0^\circ36$  and the other with  $0^\circ50$ ). We found that the  $N_p$  map of the Sano et al. (2018) velocity range prefers different normalizations inside and outside the HESS J1912+101 circle (of  $0^\circ49$  radius)<sup>10</sup>, and we allowed the normalizations to vary independently (the number of degrees of freedom is larger by one than the others). The  $\gamma$ -ray emissivity ( $\gamma$ -ray intensity per unit  $N_p$ ) inside the HESS J1912+101 circle is 2.10 times larger. The corrected  $N_p$  map, in which  $N_p$  in the annulus is scaled by  $1/2.10$  to make it compatible with a uniform CR intensity, is shown in Figure 2(d). Hereafter, we refer to this scaled map as the ‘‘Sano et al. (2018)  $N_p$  map’’. Allowing different normalizations does not improve the fit significantly for the Su et al. (2017) velocity range; therefore, the original, unscaled map is used for their velocity range. The best-fit photon index, TS, and AIC are summarized in Table 1. Therefore, all template maps significantly improve the fit (by more than  $8\sigma$ ) and yield similar values of the photon index. Among five models, the Su et al. (2017)  $N_p$  map provides the best fit to *Fermi*-LAT data, followed by the Sano et al. (2018)  $N_p$  map and the LHAASO KM2A Gaussian. These three maps imply different physical origins of the source, with the Su et al. (2017) and Sano et al. (2018)  $N_p$  maps indicating  $\gamma$ -ray emission from ISM gas at different distances and the LHAASO KM2A Gaussian representing a smooth, symmetric distribution consistent with  $\gamma$ -rays produced by IC scattering. However, they exhibit only minor differences in AIC. The spectral energy distributions (SEDs) in the LAT band of the three templates are also similar. Accordingly, we will treat them in a fair way in Section 4. We show the SED for the Sano et al. (2018)  $N_p$  map together with the TS map as a representative case in Figure 3. SEDs and TS maps of the other two templates and numerical values of the fluxes are given in Appendix 1 (Table 4 and Figure 9).

With our baseline model, the extended excess emission toward the LHAASO/H.E.S.S. source exhibits a non-uniform spatial distribution above 12.8 GeV, with a prominent peak at  $(l, b) \sim (44^\circ5, 0^\circ0)$ . The coordinate is close to the centers of HESS J1912+102 and LHAASO WCDA Gaussian, as well as the position of PSR J1913+1011. This peak-like structure persists regardless of the models adopted for the LHAASO/H.E.S.S. source counterpart. To examine this small structure, we modeled it with a uniform disk in our baseline model. Using the `extension` method<sup>11</sup> in `Fermipy`, we obtained a position of  $(l, b) = (44^\circ50 \pm 0^\circ04, 0^\circ03 \pm 0^\circ03)$  and a radius of  $0^\circ12 \pm 0^\circ03$  (Figure 1(e)). The source spectrum is hard with a photon index of  $1.76 \pm 0.05$ . However, its flux is only about 20% of the total LHAASO/H.E.S.S. source counterpart in the 10–100 GeV band, and its significance is marginal (the TS value is 10.0) even on top of our baseline model. Accordingly, we do not include this component in our spatial templates for the LHAASO/H.E.S.S. source counterpart.

Hereafter, we will first discuss the implications for CRs responsible for the overall GeV/TeV emission based on multiwavelength SED modeling in Sections 4.1–4.3, and then revisit the small peak-like structure in Section 4.4.

**Table 1.** Spatial models tested for the GeV excess toward the LHAASO/H.E.S.S. source. The values of TS and AIC are calculated with respect to the baseline model.

Model	$\Delta$ TS	$\Delta$ AIC	index
Radial Disk	98.6	88.6	$2.08 \pm 0.01$
H.E.S.S. int. map	78.6	74.6	$2.11 \pm 0.01$
Su et al. (2017) $N_p$ map	99.6	95.6	$2.08 \pm 0.01$
Sano et al. (2018) $N_p$ map	100.8	94.8	$2.06 \pm 0.01$
WCDA Gaussian	90.4	86.4	$2.09 \pm 0.01$
KM2A Gaussian	98.4	94.4	$2.08 \pm 0.01$

#### 4. DISCUSSION

Using the GeV spectrum together with data at other wavelengths, we will model the non-thermal spectrum of the LHAASO/H.E.S.S. source to investigate its  $\gamma$ -ray origin. We refrain from assuming species for the parent CRs during

<sup>10</sup> with TS=6.6 (giving  $2.5\sigma$  significance) when using the  $N_p$  maps inside the circle of  $0^\circ49$  radius and the annulus just outside instead of the single  $N_p$  map

<sup>11</sup> with the `width_max` parameter set at 0.2 (in degrees)

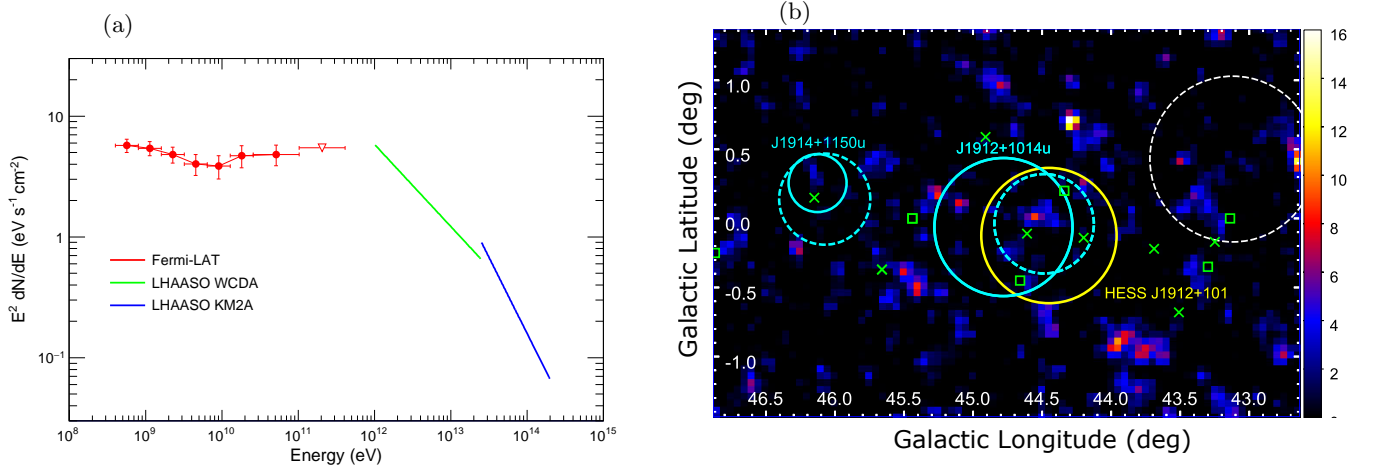


**Figure 3.** (a) *Fermi*-LAT GeV spectrum of the LHAASO/H.E.S.S. source counterpart (red points) obtained using the Sano et al. (2018)  $N_p$  map (radius of  $0.87^\circ$ ) as a template. The best-fit spectral models for LHAASO J1912+1014u, as reported by Z. Cao et al. (2024), are also plotted. (b) The TS map in  $\geq 12.8$  GeV obtained using the Sano et al. (2018)  $N_p$  map.

model fitting but employ a phenomenological approach based on observational data. Possible mechanisms for  $\gamma$ -ray radiation are the IC scattering or electron Bremsstrahlung (eB) for electrons, and neutral pion decay produced in pp collisions (pp) for protons. Which of these radiation components becomes dominant depends primarily on the electron-to-proton flux ratio ( $K_{ep}$ ) and the target gas density ( $n_{gas}$ ), as well as the energy density of the seed photon for IC. In particular, since  $K_{ep}$  and  $n_{gas}$  may vary by more than an order of magnitude depending on the assumed environment, we scan these two parameters over wide ranges,  $K_{ep} \in [10^{-5}, 10^2]$  and  $n_{gas} \in [10^{-3}, 10^3] \text{ cm}^{-3}$ , and attempt to identify viable scenarios for plausible accelerators and environments, such as an SNR (in a high gas density environment) and a PWN (in a low gas density environment).

We assume that CR spectra can be characterized by a power-law function with an exponential cutoff:  $f(E) \propto (E/E_0)^{-\alpha} \exp(-E/E_{cut})$ . We obtain the spectral index  $\alpha$ , the cutoff energy  $E_{cut}$ , and the normalizations (as the total energy of protons ( $W_p$ ) and electrons ( $W_e$ ) above 1 GeV) through SED model fitting. The spectral indices are common between CR protons and electrons, while the electron spectrum is scaled by the factor  $K_{ep}$  relative to the proton spectrum. Regarding the cutoff energies of protons ( $E_{cut,p}$ ) and electrons ( $E_{cut,e}$ ), we first consider a no-cooling case where  $E_{cut,p} = E_{cut,e}$  in Section 4.2, and then fix  $E_{cut,e}$  to a representative value in Section 4.3, because electrons undergo radiative cooling more efficiently than protons, resulting in a smaller maximum energy in SNRs (e.g., Y. Ohira et al. 2012).

#### 4.1. SED Modeling Setup

We calculate photon spectra using the Naima framework (V. Zabalza 2015). We also employ the Markov Chain Monte Carlo algorithm (D. Foreman-Mackey et al. 2013) implemented in Naima, to optimize the CR spectral parameters. This fitting takes into account the *Fermi*-LAT spectrum derived in Section 3 and the TeV measurements of HESS (H. E. S. S. Collaboration et al. 2018a), HAWC (A. U. Abeysekara et al. 2017a), and LHAASO (Z. Cao et al. 2024). For the *Fermi*-LAT GeV data points, we use the results from the Sano et al. (2018)  $N_p$  map, which agree with those from the other viable spatial templates (i.e., Su et al. (2017)  $N_p$  map and the KM2A Gaussian) within the statistical  $1\sigma$  errors. Results of the HAWC (A. U. Abeysekara et al. 2017a) and LHAASO (Z. Cao et al. 2024) measurements are reported not as data points but as fitted power-law functions, and we consider the flux and its statistical uncertainty at the normalization energy in the SED fitting.

H. Sano et al. (2018) and Y. Su et al. (2017) respectively proposed an association of HESS J1912+101 with the ISM gas in the  $23.2\text{--}26.4 \text{ km s}^{-1}$  and  $58.3\text{--}62.2 \text{ km s}^{-1}$  velocity ranges (SNR scenario). Based on the Galactic rotation curve model of J. Brand & L. Blitz (1993), the distance to the Earth is estimated to be  $1.7 \pm 0.1 \text{ kpc}$  (near side) and  $10.5 \pm 0.1 \text{ kpc}$  (far side) for the Sano et al. (2018) velocity range, whereas it is estimated to be  $4.6 \pm 0.2 \text{ kpc}$  (near side) and  $7.5 \pm 0.2 \text{ kpc}$  (far side) for the Su et al. (2017) velocity range. Alternatively, an energetic pulsar PSR J1913+1011 could accelerate electrons and positrons, producing GeV/TeV  $\gamma$ -rays; its distance is estimated at 4.5 kpc from the dispersion measure (R. N. Manchester et al. 2005). Accordingly, we adopt  $D = 1.7 \text{ kpc}$  in the following calculations, but also discuss the case of larger distances.

As for seed photon fields in the IC process, we consider the cosmic microwave background (CMB) and Galactic far-infrared (FIR) radiation. We used the interstellar radiation field model by [T. A. Porter et al. \(2017\)](#), and adopted the FIR energy density and temperature ( $0.23 \text{ eV cm}^{-3}$  and  $42.9 \text{ K}$ , respectively) at  $D = 1.7 \text{ kpc}$ . Assuming  $D = 4.6 \text{ kpc}$  gives similar values,  $0.36 \text{ eV cm}^{-3}$  and  $43.6 \text{ K}$ . Since the difference is small and the CMB photons constitute the dominant target photon field for interactions with TeV electrons, the impact on our conclusions is negligible.

For the target gas (in eB or pp processes), we estimate the number density in the vicinity of the  $\gamma$ -ray source for the [Sano et al. \(2018\)](#)  $N_p$  map. Assuming a spherical volume with a radius of  $0^\circ 87$  from the center of the H.E.S.S. source ( $l = 44^\circ 46$ ,  $b = -0^\circ 13$ ), the proton number density is found to be  $n_{\text{gas}} = 11.3 \text{ cm}^{-3}$ . The number density is  $16.2 \text{ cm}^{-3}$  for the [Su et al. \(2017\)](#)  $N_p$  map. Accordingly, we adopt  $n_{\text{gas}} = 10 \text{ cm}^{-3}$  as a nominal case.

#### 4.2. No Cooling Case

We first considered the case where  $E_{\text{cut,p}} = E_{\text{cut,e}}$ , and evaluated the CR parameters by fitting the  $\gamma$ -ray data. A summary of the parameter scan is provided in Appendix B. We identify the sets of  $n_{\text{gas}}$  and  $K_{\text{ep}}$  that lead to IC-, eB-, and pp-dominated regimes; the dominant emission process changes from IC to eB and finally to pp as  $n_{\text{gas}}/K_{\text{ep}}$  increases. In Figure 4, we present four representative cases (IC-, eB-, pp-dominated, and nominal cases) and list the model parameters in Table 2. Here, the nominal case is  $K_{\text{ep}} = 0.01$  as measured at Earth (e.g., [A. C. Cummings et al. 2016](#)) and  $n_{\text{gas}} = 10 \text{ cm}^{-2}$  as estimated by the radio data. This model reproduces the data in the *Fermi* and LHAASO KM2A bands by the pp and IC components, respectively.

All of these cases can reproduce the  $\gamma$ -ray data, but the IC-dominated case raises concerns because it requires a substantial CR energy budget,  $W_e = 7.9 \times 10^{49} (D/1.7 \text{ kpc})^2 \sim 60 \times 10^{49} (D/4.5 \text{ kpc})^2$  in erg. The most promising source of CR electrons in this region is a PWN driven by PSR J1913+1011 located at  $D \sim 4.5 \text{ kpc}$ . Indeed, this pulsar has a high spin-down luminosity of  $L_{\text{sd}} = 2.9 \times 10^{36} \text{ erg s}^{-1}$  ([D. J. Morris et al. 2002](#)), and a faint diffuse emission around the pulsar was detected at 6 GHz by [L. Duvidovich & A. Petriella \(2023\)](#), suggesting that the PWN (or TeV halo) scenario is worth considering. However, a conservative upper limit on the CR energy with the characteristic age of  $t_{\text{sd}} = 1.7 \times 10^5 \text{ yr}$  is  $L_{\text{sd}} \times t_{\text{sd}} \sim 1.5 \times 10^{49} \text{ erg}$ , which is much lower than the model requirements. Even if we adopt a distance of 1 kpc, a more energetic (or older) pulsar than PSR J1913+1011 is required.

As an alternative scenario, an SNR can be a source of CRs. Although no SNR has been identified in this region<sup>12</sup>, a typical SNR, if present, could supply up to  $\lesssim 10^{50} \text{ erg}$  ( $E_{\text{SN}}/10^{51} \text{ erg}$ ) ( $\eta/0.1$ ), where  $E_{\text{SN}}$  is the explosion energy of a supernova, and  $\eta$  is the acceleration efficiency. The CR energy for the eB-dominated case scales as  $W_e = 1.0 \times 10^{47} (n_{\text{gas}}/100 \text{ cm}^{-3})^{-1} (D/1.7 \text{ kpc})^2 \sim 1 \times 10^{48} (n_{\text{gas}}/10 \text{ cm}^{-3})^{-1} (D/1.7 \text{ kpc})^2$  in erg. For the pp-dominated case, the required energy scales as  $W_p = 1.3 \times 10^{48} (n_{\text{gas}}/100 \text{ cm}^{-3})^{-1} (D/1.7 \text{ kpc})^2 \sim 1 \times 10^{49} (n_{\text{gas}}/10 \text{ cm}^{-3})^{-1} (D/1.7 \text{ kpc})^2$  in erg. An SNR either at  $D = 1.7 \text{ kpc}$  or  $4.6 \text{ kpc}$ , as proposed by [H. Sano et al. \(2018\)](#) and [Y. Su et al. \(2017\)](#), respectively, can account for the observed  $\gamma$ -ray spectrum in terms of the energetics.

A caveat of the leptonic scenario (IC- or eB-dominated cases) is that radiative cooling of high-energy electrons poses a challenge for the required cutoff energy. Suppose that a PWN powered by the PSR J1913+1011 produce  $\gamma$  rays via IC scattering (set the energetics aside for now). If we adopt the characteristic age ( $1.7 \times 10^5 \text{ yr}$ ) and a magnetic field strength of  $6 \mu\text{G}$  comparable to the interstellar field, the maximum electron energy limited by synchrotron losses is estimated to be  $E_{\text{max,e}} \sim 2.1 \text{ TeV} (B/6 \mu\text{G})^{-2} (t_{\text{age}}/170 \text{ kyr})^{-1}$ , much smaller than the cutoff energy required by the model fitting ( $E_{\text{cut}} \sim 100 \text{ TeV}$ ; see Table 2). Alternatively,  $\gamma$  rays may be generated by an SNR via electron bremsstrahlung, and the SNR age can be estimated from the size of the remnant (e.g., [H. Suzuki et al. 2022](#); [S. Ranasinghe & D. Leahy 2023](#)). Adopting the angular diameter of the shell-like structure observed in the TeV band by the H.E.S.S. telescope ( $R_{\text{out}} = 0^\circ 49$ ; taken from Table 3 of [H. E. S. S. Collaboration et al. \(2018b\)](#)) and  $D = 1.7 \text{ kpc}$ , the diameter of the putative SNR is  $\sim 29 \text{ pc}$  ( $D/1.7 \text{ kpc}$ ). Based on the empirical relation (Eq. 2 in [S. Ranasinghe & D. Leahy 2023](#)), the SNR age will be  $\sim 13 \text{ kyr}$  ( $D/1.7 \text{ kpc}$ )<sup>2-3</sup>. Assuming this age, the maximum electron energy limited by synchrotron losses is 27 TeV, again smaller than the model requirements ( $E_{\text{cut}} \sim 50 \text{ TeV}$ ). Adopting the larger distance  $D = 4.6 \text{ kpc}$ , as proposed by [Y. Su et al. \(2017\)](#), worsens the situation.<sup>13</sup>

To assess the plausibility of the proton cutoff energy, the diffusion timescale is more important than cooling effects. According to [S. Gabici et al. \(2007\)](#), the diffusion timescale can be written as  $\tau_{\text{diff}} =$

<sup>12</sup> [N. E. Kassim \(1988\)](#) and [P. W. Gorham \(1990\)](#) reported an SNR candidate, G44.6+0.1, based on the Clark Lake survey. However, this source has not been confirmed in recent observations by [W. Reich & X.-H. Sun \(2019\)](#).

<sup>13</sup> One may argue that the uncertainty of the age-size relation (see Figure 5 in [S. Ranasinghe & D. Leahy \(2023\)](#)) may allow the age as young as 7 kyr for  $D = 1.7 \text{ kpc}$ , which is compatible with the required cutoff energy (50 TeV). Even so, the leptonic scenario is challenged by X-ray and radio upper limits, as discussed in Section 4.4.2.

11 yr  $\chi^{-1} (R/14.5 \text{ pc})^2 (E/200 \text{ TeV})^{-0.5} (B/6 \text{ } \mu\text{G})^{0.5}$ , where  $\chi$  is a parameter that represents the suppression of CR diffusion. In vicinities of CR sources such as SNRs and PWNe,  $\chi$  is theoretically expected to decrease down to  $10^{-4}$  (M. D'Angelo et al. 2018), and observationally found to be  $\lesssim 10^{-2}$  (e.g., F. Aharonian et al. 2008b; T. Oka et al. 2025; A. U. Abeysekara et al. 2017b). If we assume  $\chi = 10^{-3}$ ,  $\tau_{\text{diff}} \sim 11 \text{ kyr}$ , which is compatible with the SNR age estimated above.

In short, while we can reproduce  $\gamma$ -ray data with various spectral models, the IC-dominated case is disfavored in terms of the energetics, and the eB-dominated case is disfavored in terms of the electron cooling.

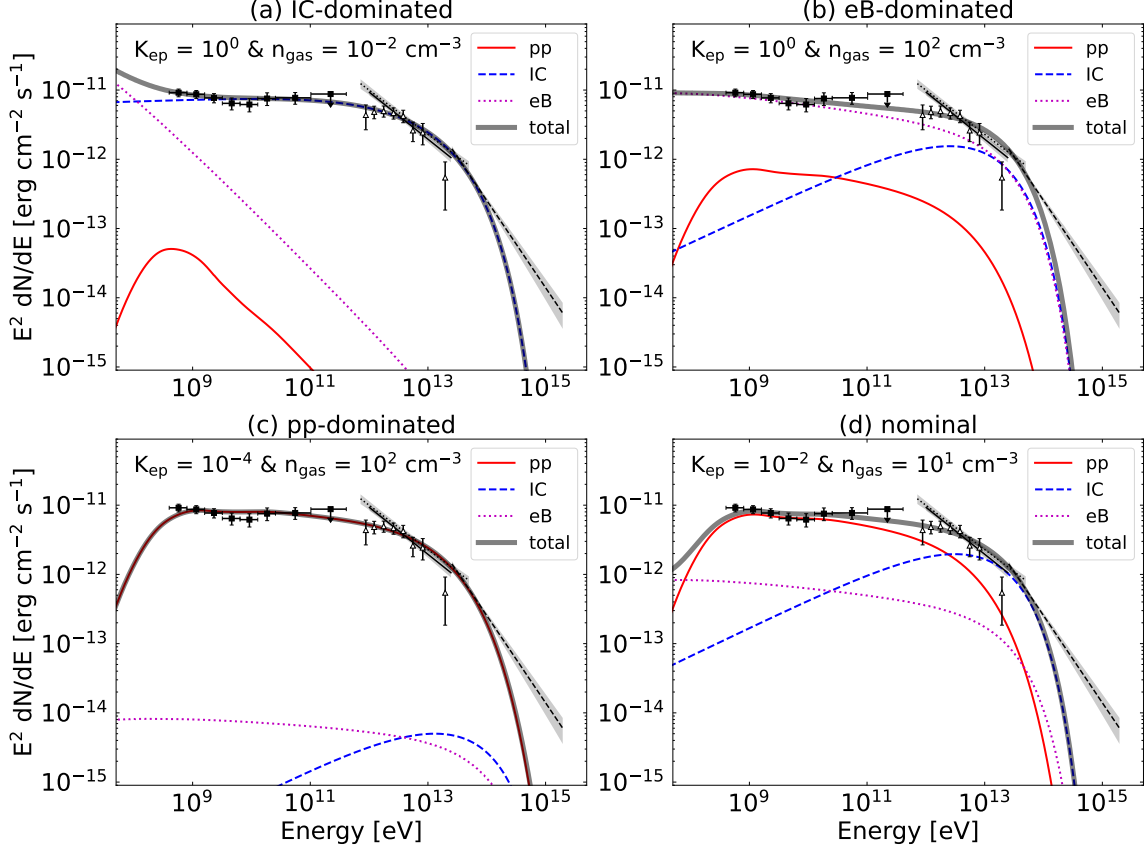


**Figure 4.** SED fit results for four representative  $K_{\text{ep}}-n_{\text{gas}}$  parameter sets assuming no electron cooling. (a) IC-dominated case with  $(K_{\text{ep}}, n_{\text{gas}}) = (10^0, 10^{-2} \text{ cm}^{-3})$ , (b) eB-dominated case with  $(K_{\text{ep}}, n_{\text{gas}}) = (10^0, 10^2 \text{ cm}^{-3})$ , (c) pp-dominated case with  $(K_{\text{ep}}, n_{\text{gas}}) = (10^{-4}, 10^2 \text{ cm}^{-3})$ , and (d) nominal case with  $(K_{\text{ep}}, n_{\text{gas}}) = (10^{-2}, 10^1 \text{ cm}^{-3})$ . In each panel, the filled squares and open triangles represent the spectrum in the *Fermi* band (this work) and the H.E.S.S. band (H. E. S. S. Collaboration et al. 2018b), respectively. The line segments show the reported spectrum by LHAASO (WCDA:1–25 TeV; KM2A:25–200 TeV). Although we account for the HAWC spectrum in the SED fitting, we do not show it (very close to the WCDA spectrum) for clarity. The red solid, blue dashed, magenta dotted, and thick black solid lines represent the spectra of pp, IC, eB, and total  $\gamma$ -ray emission, respectively.

### 4.3. Considering Cooling of CR Electrons

To resolve the inconsistency in the electron cutoff energy, we consider cases with electron cooling. We set  $E_{\text{cut},e} = 30 \text{ TeV}$ , a nominal cutoff energy for a putative SNR at  $D = 1.7 \text{ kpc}$ , and reassessed the CR parameters through the SED fitting. We found that the leptonic scenario (IC- and eB-dominated cases) inevitably fail to fit the LHAASO data of 50 TeV, whereas the pp-dominated and nominal cases can reproduce the data across the entire energy range, as shown in Figure 5. The parameters are also tabulated in Table 2. The result for the pp-dominated case is nearly the same as that obtained without electron cooling. In the nominal case, the proton cutoff energy increases by approximately a factor of five and the neutral pion decay  $\gamma$ -ray emission becomes dominant throughout the GeV and TeV band, making the source a CR proton PeVatron. Inferred spectral index is  $\sim 2.2$  and integrated energy above 1 GeV scales

**Table 2.** Parameters obtained from SED fitting for four representative cases for  $D = 1.7$  kpc. The upper rows show the results obtained with no electron cooling ( $E_{\text{cut},e} = E_{\text{cut},p}$ ), while the lower rows show those obtained by considering electron cooling with  $E_{\text{cut},e}$  fixed at 30 TeV. The errors represent the statistical  $1\sigma$  uncertainties.

	Case	$K_{\text{ep}}$	$n_{\text{gas}} [\text{cm}^{-3}]$	$W_{p,>1 \text{ GeV}} [\text{erg}]$	$\alpha$	$E_{\text{cut}} [\text{TeV}]$
no electron cooling $E_{\text{cut},e} = E_{\text{cut},p}$	IC	$10^0$	$10^{-2}$	$(7.9_{-1.1}^{+0.7}) \times 10^{49}$	$2.94_{-0.02}^{+0.02}$	$105_{-14}^{+14}$
	eB	$10^0$	$10^2$	$(1.0_{-0.1}^{+0.1}) \times 10^{47}$	$2.20_{-0.02}^{+0.02}$	$51_{-3}^{+3}$
	pp	$10^{-4}$	$10^2$	$(1.3_{-0.1}^{+0.1}) \times 10^{48}$	$2.14_{-0.02}^{+0.02}$	$205_{-18}^{+30}$
	nominal	$10^{-2}$	$10^1$	$(1.1_{-0.1}^{+0.1}) \times 10^{49}$	$2.18_{-0.02}^{+0.02}$	$58_{-4}^{+4}$
electron cooling $E_{\text{cut},e} = 30 \text{ TeV}$	pp	$10^{-4}$	$10^2$	$(1.3_{-0.1}^{+0.1}) \times 10^{48}$	$2.14_{-0.02}^{+0.02}$	$200_{-17}^{+17}$
	nominal	$10^{-2}$	$10^1$	$(1.1_{-0.1}^{+0.1}) \times 10^{49}$	$2.20_{-0.02}^{+0.02}$	$320_{-50}^{+50}$

NOTE— For the leptonic scenario (IC- and eB-dominated cases),  $W_{e,>1 \text{ GeV}}$  is equal to  $W_{p,>1 \text{ GeV}}$ .

as  $W_p = 1.1 \times 10^{49} (n_{\text{gas}}/10 \text{ cm}^{-3})^{-1} (D/1.7 \text{ kpc})^2$  in erg. This gives  $W_p$  of  $\sim 1 \times 10^{49}$  erg and  $\sim 5 \times 10^{49}$  erg for the Sano et al. (2018)  $N_p$  map and Su et al. (2017)  $N_p$  map, respectively.

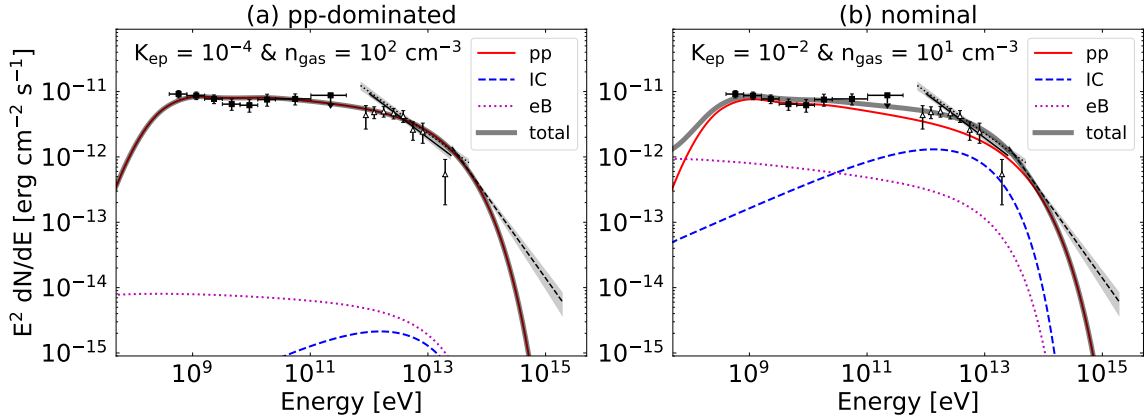


**Figure 5.** SED fit results for two representative  $K_{\text{ep}}-n_{\text{gas}}$  parameter sets assuming electron cooling with  $E_{\text{cut},e}$  fixed to 30 TeV. (a) pp-dominated case with  $(K_{\text{ep}}, n_{\text{gas}}) = (10^{-4}, 10^2 \text{ cm}^{-3})$ , and (b) nominal case with  $(K_{\text{ep}}, n_{\text{gas}}) = (10^{-2}, 10^1 \text{ cm}^{-3})$ . See the caption of Figure 4 for the meanings of lines and markers.

Taking into account the electron cooling also affects the energy dependence of the relative contribution of each emission component (IC, eB, and pp) in the nominal case (Figure 6). With  $E_{\text{cut},e} = 30 \text{ TeV}$ , the IC-to-pp flux ratio is largest between 1 and 10 TeV, which coincides with the energy range observed by H.E.S.S. and LHAASO WCDA. Figure 6 implies that while the  $\gamma$ -ray morphology traces the dense gas distribution in GeV and  $>50 \text{ TeV}$  energies, it may be affected by the increasing contribution from IC emission in 1–10 TeV. This energy dependence could account for the lower TS values with the H.E.S.S. intensity map and the WCDA Gaussian template (Table 1).

#### 4.4. Constraints from X-ray and Radio Data

Although the hadronic scenario is preferred for energetics and cooling, the leptonic scenario remains viable if a putative pulsar is more energetic (or older), or a putative SNR is younger. If part of the  $\gamma$ -ray emission originates from the accelerated electrons, synchrotron emission is expected from the radio to X-ray band. A stringent radio upper limit for the counterpart of HESS J1912+101 was reported from radio polarization observation by W. Reich & X.-H. Sun (2019). In the following, we first search for the X-ray counterpart (Section 4.4.1) and then discuss constraints on the leptonic scenario from X-ray and radio data (Section 4.4.2).

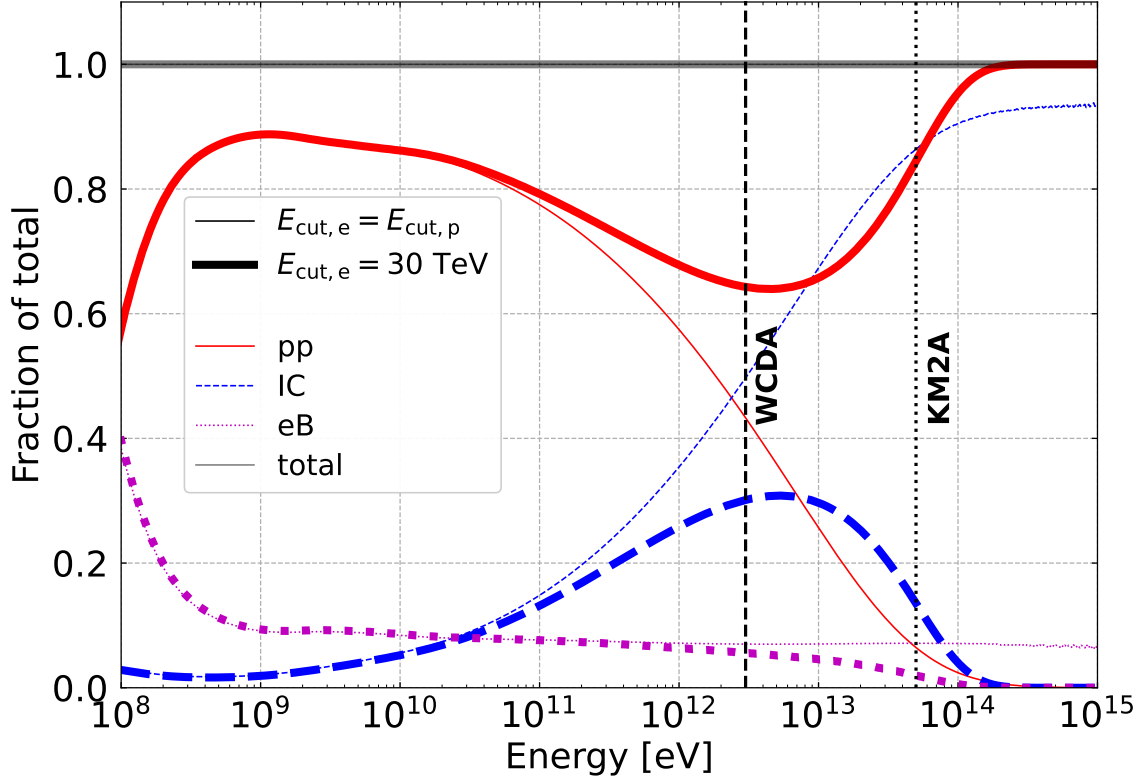


**Figure 6.** Relative contribution by each emission component (IC, eB, and pp) in the nominal case. Thin lines and thick lines show the results with  $E_{\text{cut},e} = E_{\text{cut},p}$  and  $E_{\text{cut},e} = 30 \text{ TeV}$ , respectively. The dashed and dotted vertical lines indicate the normalization energies of the fitted functions for WCDA and KM2A, as reported in Z. Cao et al. (2024).

#### 4.4.1. Search for X-ray Counterpart

As discussed in Section 3.2, we identified a small peak-like structure at  $(l, b) \sim (44^\circ 50, 0^\circ 03)$  with a radius of  $\sim 0''.12$  (Figure 1(e)), located near the center of the overall excess. Assuming that this feature originates from an unknown PWN via IC scattering, we searched for an X-ray counterpart using archival Chandra data. We used the Chandra data ObsID 3854, which partially covers the vicinity of the position  $(l, b) = (44^\circ 50, 0^\circ 03)$ . Here, we consider a  $0''.12$ -radius circle that is partially covered by the ACIS-I2, S1, and S2 chips. The effective exposure, after reprocessing with `chandra_repro` in the CIAO package v4.16 (A. Fruscione et al. 2006), is  $\sim 20$  ks. We confirmed that there is no visible diffuse emission within the circular region relative to the background. (Figure 7 (a)) We note that PSR J1913+1011 was not detected in the Chandra data, as only an upper limit on the flux is reported by C. Chang et al. (2008). On the other hand, two sources CXOU J191240.6+101755 at  $(l, b) = (44^\circ 50'56.6, 0^\circ 02'79.0)$  and CXOU J191238.0+101043 at  $(l, b) = (44^\circ 39'43.9, -00^\circ 01'81.6)$  are located in this region (C. Chang et al. 2008). We found that they are both significantly extended relative to the Chandra point spread function with the source extents of  $\sim 5''$  when modeled with a single Gaussian (Table 3), suggesting they may be unknown PWNe. We note that the radial distribution of CXOU J191238.0+101043 is flatter than a single Gaussian function in radii larger than  $5''$ . We then extracted the Chandra spectra from a  $19''$  radius circle centered on these sources. We performed a simple phenomenological fit with a power-law model in the 1–5 keV band, where the background is nearly negligible. We used XSPEC version 12.14.1 (K. A. Arnaud 1996) for the spectroscopy. The derived flux in the 2–10 keV band and power-law index are  $\sim 1.5 \times 10^{-14} \text{ erg s}^{-1} \text{ cm}^{-2}$  and  $\sim 2.6$  for CXOU J191240.6+101755, and  $\sim 60 \times 10^{-14} \text{ erg s}^{-1} \text{ cm}^{-2}$  and  $\sim 0.5$  for CXOU J191238.0+101043, respectively (Table 3). The observed low flux ( $\sim 1/100$  of the flux of hard excess in 10–100 GeV) and soft X-ray spectrum of CXOU J191240.6+101755 could be consistently explained by synchrotron (radio to X-ray) and IC ( $\gamma$ -ray) scenarios with small magnetic-field values and a synchrotron emission cutoff at  $\leq 1 \text{ keV}$ . Even so, the source’s contribution to the entire  $\gamma$ -ray excess emission in the 10–100 GeV range is at the 20% level. Another source, CXOU J191238.0+101043 is unrelated to the  $\gamma$ -ray excess, with a very hard X-ray spectrum that

contradicts the spectral index ( $\sim 2$ ) of the GeV excess. Accordingly, we will not further consider these sources as potential counterparts of the entire  $\gamma$ -ray excess.

**Table 3.** Parameters of CXOU J191240.6+101755 and CXOU J191238.0+101043

Source	Power-law index	2–10 keV flux ( $10^{-14}$ erg s $^{-1}$ cm $^{-2}$ )	Gaussian sigma ( $''$ )
CXOU J191240.6+101755	$2.6 \pm 0.4$	$1.5 \pm 0.3$	$6.0 \pm 1.2$
CXOU J191238.0+101043	$0.45 \pm 0.14$	$60 \pm 8$	$3.8 \pm 0.4$

We then evaluated the maximum allowed non-thermal diffuse X-ray emission in this region by modeling the sky and particle-induced backgrounds, following the methodology used in recent work on faint diffuse sources (e.g., [H. Suzuki et al. 2020, 2025](#); [Y. Kuboike et al. 2025](#)). We extracted the X-ray spectrum from a  $0^\circ 12$ -radius circle centered on  $(l, b)=(44^\circ 50, 0^\circ 03)$ . We used the `mkacisback` tool v2023-09-23 ([H. Suzuki et al. 2021](#)), to generate the expected particle-induced background spectrum for this region. As for the sky background, we considered the Local hot bubble (foreground emission), the Milky Way halo, the Cosmic X-ray background, and the Galactic ridge X-ray emission. The first two were modeled using the collisional ionization equilibrium plasma model (`apec` in XSPEC) with electron temperatures of 0.1 keV and 0.7 keV, respectively. The Cosmic X-ray background component was modeled as a power law with a slope of 1.42 and a surface brightness of  $5.4 \times 10^{-15}$  erg cm $^{-2}$  arcmin $^{-2}$ . The Galactic ridge emission is modeled using an `apec` model with an electron temperature of 6.6 keV and a fixed flux, calculated based on [H. Uchiyama et al. \(2013\)](#). Following [H. Uchiyama et al. \(2013\)](#), we assumed a  $\pm 20\%$  uncertainty for the flux. We then modeled the presumable non-thermal X-ray emission associated with the  $\gamma$ -ray excess using a power-law model (slope fixed at 2.0). We applied the free Galactic absorption (`tbabs` model in XSPEC) to the sky components other than the Local hot bubble. We found that this spectral model reasonably explains the data in the 0.5–10.0 keV band, as shown in Figure 7 (b). The 95% upper limit flux of the power-law model in the 2–10 keV band was derived to be  $\sim 1 \times 10^{-13}$  erg s $^{-1}$  cm $^{-2}$  for the entire analysis region (area = 84.5 arcmin $^2$ ), corresponding to a surface brightness of  $\sim 1 \times 10^{-15}$  erg s $^{-1}$  cm $^{-2}$  arcmin $^{-2}$ . The Galactic absorption column density was determined to be  $\sim 1 \times 10^{22}$  cm $^{-2}$ , which is reasonable considering the source location ([HI4PI Collaboration et al. 2016](#); [P. M. W. Kalberla et al. 2005](#); [J. M. Dickey & F. J. Lockman 1990](#)). Since this upper limit is mainly determined by the uncertainty in the background (Galactic ridge X-ray emission), we can scale it to the entire area of the LHAASO/H.E.S.S. source. If we assume the size of HESS J1912+101 ( $0^\circ 49$  radius), the upper limit will be  $\sim 2 \times 10^{-12}$  erg s $^{-1}$  cm $^{-2}$  in the SED.

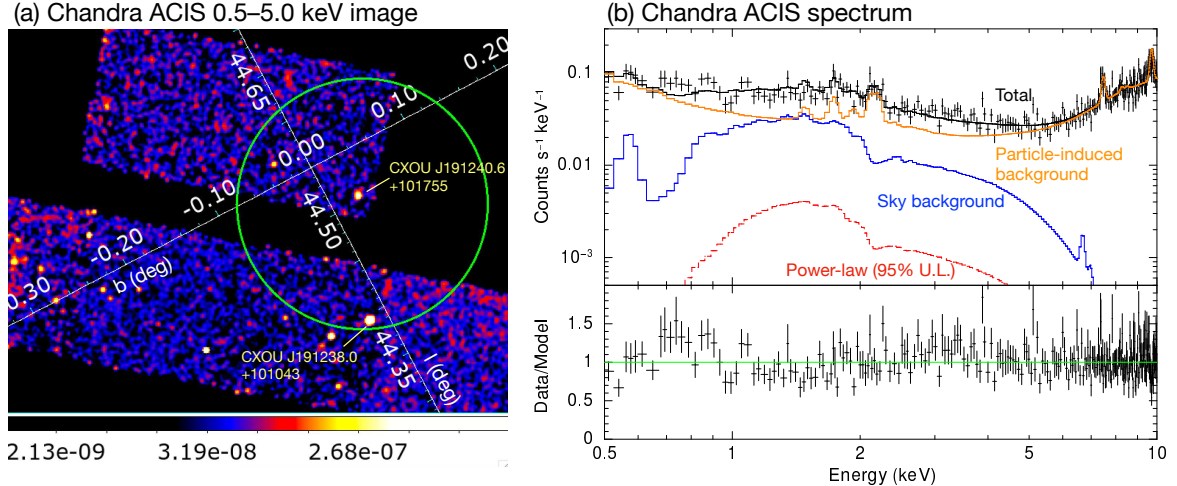


**Figure 7.** (a) A 0.5–5.0 keV Chandra image and (b) energy spectrum with the best-fit spectral model. The spectrum was extracted from the green circle in panel (a). The blue, orange, and black lines indicate the sky background, particle-induced background, and total model, respectively. The upper limit for the power-law component, used as the counterpart to the  $\gamma$ -ray excess, is shown by the red dashed line.

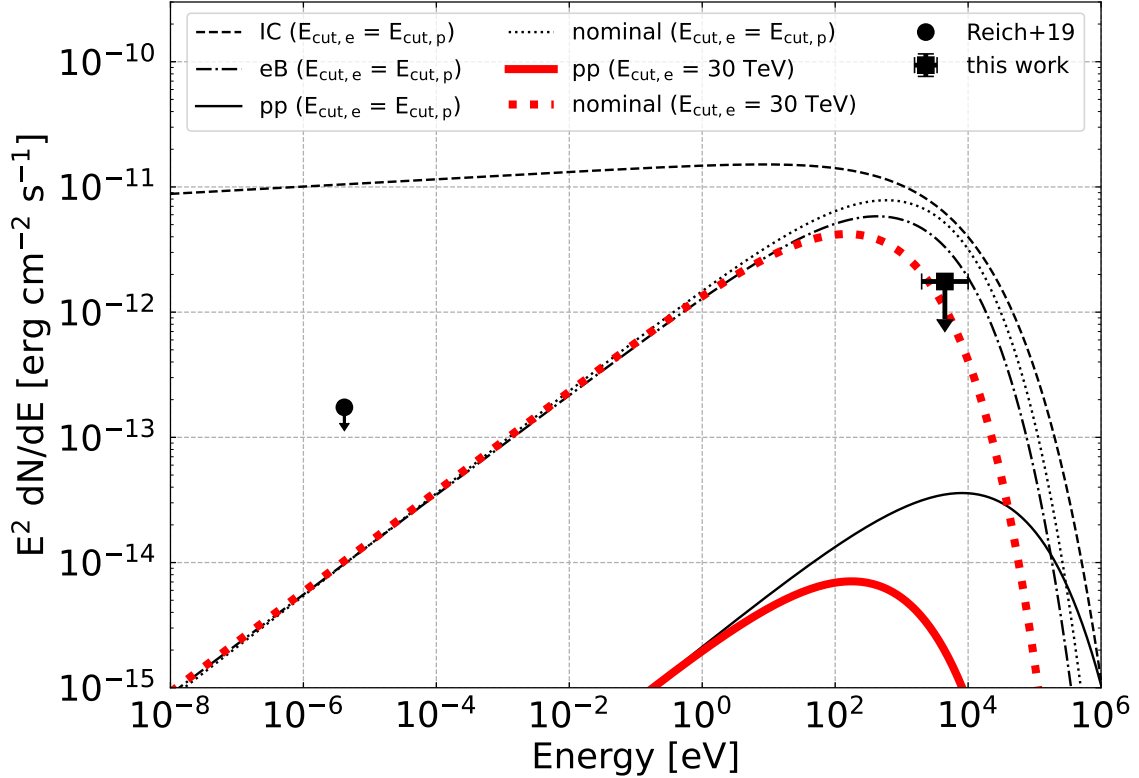


**Figure 8.** Synchrotron spectra of each representative case. The dashed, dot-dashed, solid, and dotted lines represent the IC-dominated, eB-dominated, pp-dominated, and nominal cases, respectively. The thick red and thin black lines indicate the cases with  $E_{\text{cut},e} = E_{\text{cut},p}$  and  $E_{\text{cut},e} = 30$  TeV, respectively. The circle shows the upper limit taken from [W. Reich & X.-H. Sun \(2019\)](#), while the square shows the upper limit derived in this work.

#### 4.4.2. Limits on the Leptonic Scenario

Although we were unable to detect enhanced diffuse X-ray emission, we obtained a tight upper limit. Together with the previously reported radio upper limit, this further constrains the leptonic scenario.

We calculated synchrotron spectra for each representative case. Figure 8 shows a comparison between the synchrotron spectra and the upper limits in the X-ray and radio bands, the latter of which is taken from [W. Reich & X.-H. Sun \(2019\)](#). If we assume a magnetic-field strength of  $6 \mu\text{G}$ , typical of that in the cold atomic or molecular clouds with  $n_{\text{gas}} \leq 300 \text{ cm}^{-3}$  ([C. Heiles & T. H. Troland 2005](#); [R. M. Crutcher 2012](#)), the IC-, eB-dominated cases and the nominal case with  $E_{\text{cut},e} = E_{\text{cut},p}$  are incompatible with the X-ray upper limit. The IC-dominated case is also inconsistent with the radio upper limit, requiring an unrealistically low magnetic field below  $1 \mu\text{G}$ . These constraints effectively exclude the leptonic scenario in a typical magnetic field environment, reinforcing the proton PeVatron scenario for the LHAASO/H.E.S.S. source.

It should be noted that the magnetic field strength can be lower than the typical interstellar value, particularly in low-density environments (e.g., [A. Seta & N. M. McClure-Griffiths 2025](#)). A PWN powered by PSR J1849-0001 is an example ([The LHAASO Collaboration 2026](#)). If the magnetic field strength is as low as  $3 \mu\text{G}$ , all representative cases are consistent with the X-ray upper limit, making the eB-dominated case plausible. However, the high gas density implicitly assumed in the eB-dominated case is incompatible with the required low magnetic-field value. In the IC-dominated case, the compatibility with radio and X-ray upper limits is achieved if the magnetic field is extremely low ( $\leq 1 \mu\text{G}$ ). Alternatively, a moderately low magnetic field ( $\sim 3 \mu\text{G}$ ) combined with a low-energy break in synchrotron emission at  $\sim 10^{-3}$  eV, as observed in middle-aged PWN systems (e.g., [T. Temim et al. 2013, 2015](#); [Y. Gong et al. 2025](#)), also satisfies these constraints. We remind that although the IC-dominated case aligns with radio and X-ray data under these configurations, it remains severely challenged by energetic considerations (see Section 4.2).

In summary, while the leptonic scenario cannot be formally excluded, the hadronic scenario offers a more natural explanation for the observed data in the radio and X-ray bands as well as GeV and TeV  $\gamma$ -ray bands.

## 5. SUMMARY AND PROSPECTS

LHAASO has reported more than 40 sub-PeV sources, which are promising candidates for either proton or electron PeVatron. Multi-wavelength observations are crucial for identifying the dominant particle species and evaluating the CR energy content of these objects. In this study, we investigated the LHAASO J1912+1014u (and HESS J1912+101) region using *Fermi*-LAT GeV  $\gamma$ -ray data and FUGIN CO data to assess the proton PeVatron scenario.

We analyzed 15 years of *Fermi*-LAT data in the 0.4–409.6 GeV range. By improving the standard *Fermi*-LAT diffuse emission model, we substantially reduced the large residuals that appear when using the standard diffuse model. This allowed us to reveal a significant excess above the diffuse background and nearby source models, likely representing  $\geq 10$  GeV emission associated with the LHAASO/H.E.S.S. source. The GeV emission exhibits a hard spectrum (index of  $\sim 2.1$ ) and is well modeled using ISM gas templates with velocities of about  $25 \text{ km s}^{-1}$  or  $60 \text{ km s}^{-1}$ .

Using the GeV spectrum together with the reported TeV measurements, we have phenomenologically evaluated the CR spectra responsible for the LHAASO/H.E.S.S. source. By exploring combinations of  $K_{\text{ep}}$  and  $n_{\text{gas}}$ , we have identified parameter sets in which the IC, eB, and pp emission components become dominant, respectively. In the observationally motivated nominal case ( $K_{\text{ep}} = 1\%$ ,  $n_{\text{gas}} = 10 \text{ cm}^{-3}$ ), the pp and IC components contribute at comparable levels.

Considerations of the CR energy budget disfavor the IC-dominated case. Although the eB-dominated case is energetically viable, the electron cutoff energy required to reproduce the GeV–TeV  $\gamma$ -ray spectrum exceeds the maximum energy expected from radiative cooling for the age of a putative SNR. When adopting a plausible electron cutoff energy of  $E_{\text{cut,e}} = 30 \text{ TeV}$ , the leptonic scenarios (IC- and eB-dominated cases) become inconsistent with the data. In the nominal case, the IC contribution is substantial only in the 1–10 TeV energy range, indicating that the source is predominantly powered by hadronic processes. The inferred CR proton spectral index is  $\sim 2.2$ , and the total CR proton energy above 1 GeV is  $(1\text{--}5) \times 10^{49} \text{ erg}$ , depending on the assumed distance of the source.

We further found that, under a typical interstellar magnetic field of  $6 \mu\text{G}$ , the synchrotron emission predicted in the IC-dominated, eB-dominated, and nominal no-cooling cases exceeds the upper limit on diffuse X-ray emission. This provides additional support for the proton PeVatron scenario.

In conclusion, the nominal case including electron cooling offers the most self-consistent explanation of both the multi-wavelength spectral data and the GeV–TeV spatial morphology, strongly favoring the proton PeVatron scenario. As demonstrated in this work, detailed comparisons between ISM gas distributions and *Fermi*-LAT  $\gamma$ -ray data are crucial for identifying the particle species and constraining the CR properties of sub-PeV sources. Radio and X-ray observations, whether detections or upper limits, also provide valuable constraints. We note that our estimate of the electron cutoff energy is limited by the currently available data, and that the LHAASO KM2A spectrum, reported as a simple power-law model, was incorporated approximately in our SED modeling. Deeper observations from radio to TeV  $\gamma$ -ray will be essential for fully characterizing this object and advancing our understanding of the origin of Galactic CRs up to the knee energy.

## ACKNOWLEDGMENTS

The *Fermi* LAT Collaboration acknowledges generous ongoing support from a number of agencies and institutes that have supported both the development and the operation of the LAT as well as scientific data analysis. These include the National Aeronautics and Space Administration and the Department of Energy in the United States, the Commissariat à l’Energie Atomique and the Centre National de la Recherche Scientifique / Institut National de Physique Nucléaire et de Physique des Particules in France, the Agenzia Spaziale Italiana and the Istituto Nazionale di Fisica Nucleare in Italy, the Ministry of Education, Culture, Sports, Science and Technology (MEXT), High Energy Accelerator Research Organization (KEK) and Japan Aerospace Exploration Agency (JAXA) in Japan, and the K. A. Wallenberg Foundation, the Swedish Research Council and the Swedish National Space Board in Sweden.

Additional support for science analysis during the operations phase is gratefully acknowledged from the Istituto Nazionale di Astrofisica in Italy and the Centre National d’Études Spatiales in France. This work performed in part under DOE Contract DE-AC02-76SF00515.

This work was also supported in part by a University Research Support Grant from the National Astronomical Observatory of Japan (NAOJ).

Part of this work was supported by JSPS KAKENHI Grant Numbers 23K25882 and 23H04895 (T. Mizuno), 22H00152 and 24H00246 (H. Sano), and 24K17093 (H. Suzuki).

This paper employs a list of Chandra datasets, obtained by the Chandra X-ray Observatory, contained in DOI: [10.25574/cdc.578](https://doi.org/10.25574/cdc.578).

#### AUTHOR CONTRIBUTIONS

T. Mizuno and N. Nakahara analyzed *Fermi*-LAT  $\gamma$ -ray data and investigated the spectrum and morphology of the source. H. Sano and T. Murase reprocessed FUGIN CO data and prepared target-gas maps, including contributions from optically thick H I. H. Suzuki analyzed Chandra data and constrained the diffuse X-ray emission from the source by accounting for astrophysical and instrumental backgrounds. T. Oka carried out SED modeling by performing a comprehensive fit to the multiwavelength data. All coauthors participated in interpreting the results and providing feedback to the manuscript.

*Facilities:* *Fermi*-LAT, CXO, Nobeyama 45-m radio telescope (NRO45), The Very Large Array (VLA)

*Software:* FermiTools ( Fermi Science Support Development Team 2019), Fermipy (M. Wood et al. 2017), Naima (V. Zabalza 2015), astropy ( Astropy Collaboration et al. 2013, 2018, 2022), numpy (C. R. Harris et al. 2020), Scipy (P. Virtanen et al. 2020). XSPEC (K. A. Arnaud 1996), CIAO (A. Fruscione et al. 2006), mkacispack (H. Suzuki et al. 2021)

#### APPENDIX

##### A. SUMMARY OF *FERMI*-LAT SPECTRUM

We give the numerical values of the SEDs in the LAT band (Table 4). We also show the SED plot and TS map for the Su et al. (2017)  $N_p$  map and LHAASO KM2A Gaussian (Figure 9).

**Table 4.** Spectrum of the GeV excess toward the LHAASO/H.E.S.S. source

Energy (GeV)	KM2A Gaussian	Su et al. (2017) $N_p$ map	Sano et al. (2018) $N_p$ map
	$(10^{-9} \text{ GeV s}^{-1} \text{ cm}^{-2})$		
0.4–0.8	$6.13 \pm 0.77$	$5.85 \pm 0.74$	$5.72 \pm 0.73$
0.8–1.6	$6.13 \pm 0.78$	$5.49 \pm 0.74$	$5.42 \pm 0.72$
1.6–3.2	$5.54 \pm 0.81$	$4.65 \pm 0.76$	$4.81 \pm 0.73$
3.2–6.4	$4.09 \pm 0.88$	$4.12 \pm 0.81$	$4.01 \pm 0.78$
6.4–12.8	$4.77 \pm 0.97$	$3.67 \pm 0.87$	$3.86 \pm 0.84$
12.8–25.6	$5.89 \pm 1.16$	$4.66 \pm 1.01$	$4.71 \pm 0.98$
25.6–102.4	$4.70 \pm 1.06$	$4.99 \pm 0.94$	$4.82 \pm 0.92$
102.4–409.6	$\leq 5.73$	$\leq 5.62$	$\leq 5.47$

##### B. SUMMARY OF CR PARAMETER SCAN

Figure 10 summarizes the parameter scan for the no-cooling case, showing the best-fit values of  $W_p$ ,  $W_e$ , index, and  $E_{\text{cut}}$  as a function of  $K_{\text{ep}}$  and  $n_{\text{gas}}$ . Interestingly, the panel of  $E_{\text{cut}}$  is divided into three distinct layers, with a boundary at  $\sim 80$  TeV. As  $n_{\text{gas}}/K_{\text{ep}}$  increases, the dominant emission process changes from IC to eB, and finally to pp. The nominal case lies near the boundary between the eB-dominated and pp-dominated regimes.

#### REFERENCES

- Abdollahi, S., Acero, F., Baldini, L., et al. 2022, ApJS, 260, 53, doi: [10.3847/1538-4365/ac6751](https://doi.org/10.3847/1538-4365/ac6751),  
 Abeysekera, A. U., Albert, A., Alfaro, R., et al. 2017a, ApJ, 843, 40, doi: [10.3847/1538-4357/aa7556](https://doi.org/10.3847/1538-4357/aa7556)

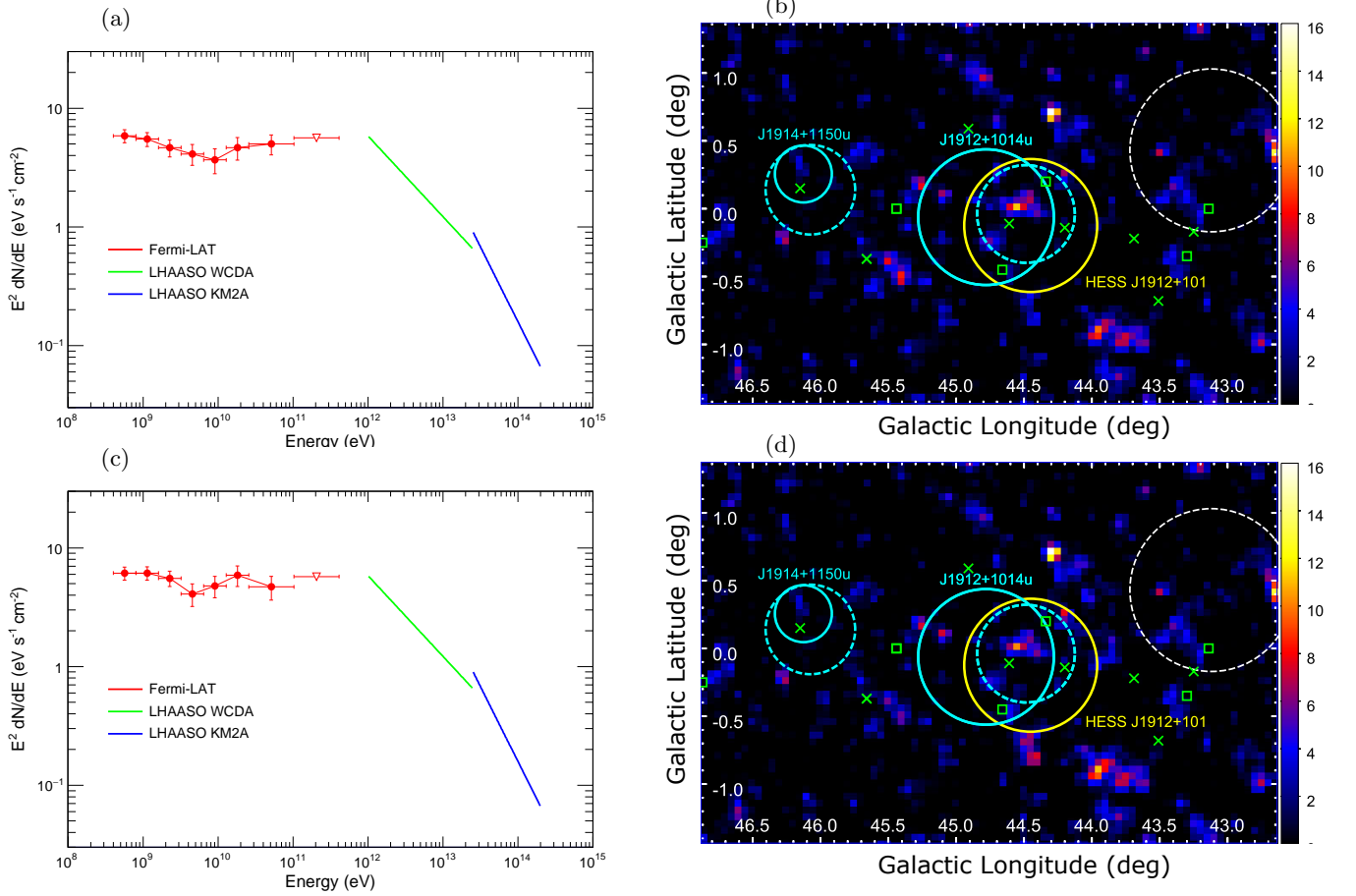


**Figure 9.** (a) *Fermi*-LAT GeV spectrum of the LHAASO/H.E.S.S. source counterpart (red points) obtained using the Su et al. (2017)  $N_p$  map (radius of  $0.87$ ) as a template. The best-fit spectral models for LHAASO J1912+1014u in Z. Cao et al. (2024) are also plotted. (b) The TS map in  $\geq 12.8$  GeV obtained using the Su et al. (2017)  $N_p$  map. (c) and (d) are the same as panels (a) and (b), respectively, but obtained using LHAASO KM2A Gaussian.

Abeysekera, A. U., Albert, A., Alfaro, R., et al. 2017b, *Science*, 358, 911, doi: [10.1126/science.aan4880](https://doi.org/10.1126/science.aan4880)

Aharonian, F., Akhperjanian, A. G., Barres de Almeida, U., et al. 2008a, *A&A*, 484, 435, doi: [10.1051/0004-6361:20078715](https://doi.org/10.1051/0004-6361:20078715)

Aharonian, F., Akhperjanian, A. G., Bazer-Bachi, A. R., et al. 2008b, *A&A*, 481, 401, doi: [10.1051/0004-6361:20077765](https://doi.org/10.1051/0004-6361:20077765)

Arnaud, K. A. 1996, in *Astronomical Society of the Pacific Conference Series*, Vol. 101, *Astronomical Data Analysis Software and Systems V*, ed. G. H. Jacoby & J. Barnes, 17

Astropy Collaboration, Robitaille, T. P., Tollerud, E. J., et al. 2013, *A&A*, 558, A33, doi: [10.1051/0004-6361/201322068](https://doi.org/10.1051/0004-6361/201322068)

Astropy Collaboration, Price-Whelan, A. M., Sipőcz, B. M., et al. 2018, *AJ*, 156, 123, doi: [10.3847/1538-3881/aabc4f](https://doi.org/10.3847/1538-3881/aabc4f)

Astropy Collaboration, Price-Whelan, A. M., Lim, P. L., et al. 2022, *ApJ*, 935, 167, doi: [10.3847/1538-4357/ac7c74](https://doi.org/10.3847/1538-4357/ac7c74)

Atwood, W., Albert, A., Baldini, L., et al. 2013, arXiv e-prints, arXiv:1303.3514, doi: [10.48550/arXiv.1303.3514](https://doi.org/10.48550/arXiv.1303.3514)

Atwood, W. B., Abdo, A. A., Ackermann, M., et al. 2009, *ApJ*, 697, 1071, doi: [10.1088/0004-637X/697/2/1071](https://doi.org/10.1088/0004-637X/697/2/1071)

Ballet, J., Bruel, P., Burnett, T. H., Lott, B., & The *Fermi*-LAT collaboration. 2023, arXiv e-prints, arXiv:2307.12546, doi: [10.48550/arXiv.2307.12546](https://doi.org/10.48550/arXiv.2307.12546)

Bertsch, D. L., Dame, T. M., Fichtel, C. E., et al. 1993, *ApJ*, 416, 587, doi: [10.1086/173261](https://doi.org/10.1086/173261)

Brand, J., & Blitz, L. 1993, *A&A*, 275, 67

Bruel, P., Burnett, T. H., Digel, S. W., et al. 2018, arXiv e-prints, arXiv:1810.11394, doi: [10.48550/arXiv.1810.11394](https://doi.org/10.48550/arXiv.1810.11394)

Cao, Z., Aharonian, F., An, Q., et al. 2024, *ApJS*, 271, 25, doi: [10.3847/1538-4365/acfd29](https://doi.org/10.3847/1538-4365/acfd29)

Chang, C., Konopelko, A., & Cui, W. 2008, *ApJ*, 682, 1177, doi: [10.1086/589225](https://doi.org/10.1086/589225)

Crutcher, R. M. 2012, *ARA&A*, 50, 29, doi: [10.1146/annurev-astro-081811-125514](https://doi.org/10.1146/annurev-astro-081811-125514)

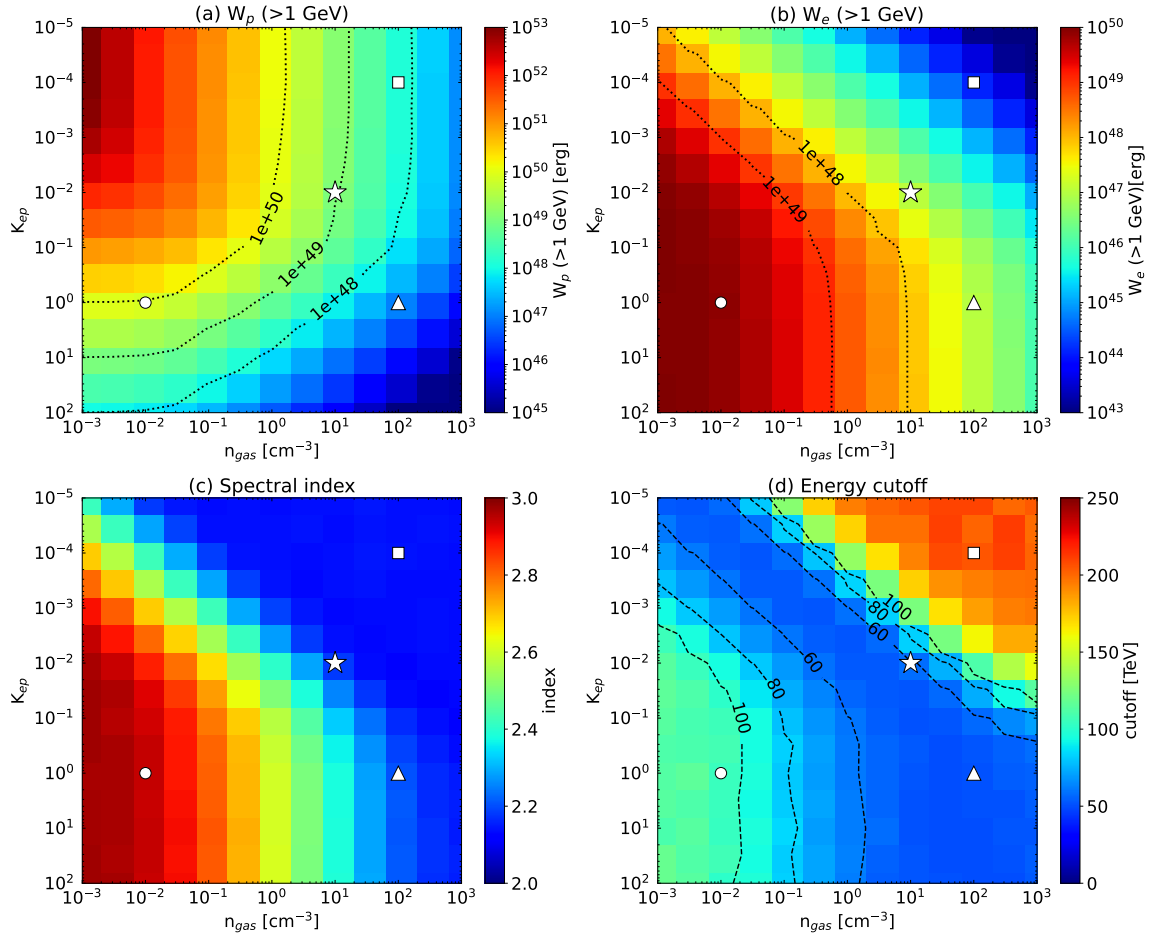


**Figure 10.** Summary of the parameter scan with no electron cooling: (a)  $W_p$ , (b)  $W_e$ , (c) spectral index, and (d)  $E_{\text{cut}}$ . The white circle, triangle, square, and star represent  $K_{\text{ep}}$  and  $n_{\text{gas}}$  for IC-, eB-, pp-dominated, and nominal cases.

Cummings, A. C., Stone, E. C., Heikkilä, B. C., et al. 2016,

ApJ, 831, 18, doi: [10.3847/0004-637X/831/1/18](https://doi.org/10.3847/0004-637X/831/1/18)

Dame, T. M., Hartmann, D., & Thaddeus, P. 2001, ApJ,

547, 792, doi: [10.1086/318388](https://doi.org/10.1086/318388)

D'Angelo, M., Morlino, G., Amato, E., & Blasi, P. 2018,

MNRAS, 474, 1944, doi: [10.1093/mnras/stx2828](https://doi.org/10.1093/mnras/stx2828)

Dickey, J. M., & Lockman, F. J. 1990, ARA&A, 28, 215,

doi: [10.1146/annurev.aa.28.090190.001243](https://doi.org/10.1146/annurev.aa.28.090190.001243)

Duvidovich, L., & Petriella, A. 2023, A&A, 672, A195,

doi: [10.1051/0004-6361/202245819](https://doi.org/10.1051/0004-6361/202245819)

Fermi Science Support Development Team. 2019,

Fermitools: Fermi Science Tools,, Astrophysics Source Code Library, record ascl:1905.011

<http://ascl.net/1905.011>

Foreman-Mackey, D., Hogg, D. W., Lang, D., & Goodman,

J. 2013, PASP, 125, 306, doi: [10.1086/670067](https://doi.org/10.1086/670067)

Fruscione, A., McDowell, J. C., Allen, G. E., et al. 2006, in

Society of Photo-Optical Instrumentation Engineers (SPIE) Conference Series, Vol. 6270, Observatory Operations: Strategies, Processes, and Systems, ed. D. R. Silva & R. E. Doxsey, 62701V, doi: [10.1117/12.671760](https://doi.org/10.1117/12.671760)

Fukui, Y., Torii, K., Onishi, T., et al. 2015, ApJ, 798, 6,

doi: [10.1088/0004-637X/798/1/6](https://doi.org/10.1088/0004-637X/798/1/6)

Fukui, Y., Okamoto, R., Kaji, R., et al. 2014, The

Astrophysical Journal, 796, 59, doi: [10.1088/0004-637X/796/1/59](https://doi.org/10.1088/0004-637X/796/1/59)

Fukui, Y., Sano, H., Sato, J., et al. 2017, ApJ, 850, 71,

doi: [10.3847/1538-4357/aa9219](https://doi.org/10.3847/1538-4357/aa9219)

Gabici, S., Aharonian, F. A., & Blasi, P. 2007, Ap&SS, 309,

365, doi: [10.1007/s10509-007-9427-6](https://doi.org/10.1007/s10509-007-9427-6)

Gong, Y., Zhou, L., Xia, Q., et al. 2025, ApJ, 981, 7,

doi: [10.3847/1538-4357/adae90](https://doi.org/10.3847/1538-4357/adae90)

Gorham, P. W. 1990, ApJ, 364, 187, doi: [10.1086/169401](https://doi.org/10.1086/169401)

H. E. S. S. Collaboration, Abdalla, H., Abramowski, A.,

et al. 2018a, A&A, 612, A1, doi: [10.1051/0004-6361/201732098](https://doi.org/10.1051/0004-6361/201732098)

- H. E. S. S. Collaboration, Abdalla, H., Abramowski, A., et al. 2018b, *A&A*, 612, A8, doi: [10.1051/0004-6361/201730737](https://doi.org/10.1051/0004-6361/201730737)
- Harris, C. R., Millman, K. J., van der Walt, S. J., et al. 2020, *Nature*, 585, 357, doi: [10.1038/s41586-020-2649-2](https://doi.org/10.1038/s41586-020-2649-2)
- Heiles, C., & Troland, T. H. 2005, *ApJ*, 624, 773, doi: [10.1086/428896](https://doi.org/10.1086/428896)
- HI4PI Collaboration, Ben Bekhti, N., Flöer, L., et al. 2016, *A&A*, 594, A116, doi: [10.1051/0004-6361/201629178](https://doi.org/10.1051/0004-6361/201629178)
- Kalberla, P. M. W., Burton, W. B., Hartmann, D., et al. 2005, *A&A*, 440, 775, doi: [10.1051/0004-6361:20041864](https://doi.org/10.1051/0004-6361:20041864)
- Kassim, N. E. 1988, *ApJL*, 328, L55, doi: [10.1086/185159](https://doi.org/10.1086/185159)
- Kuboike, Y., Sato, T., Suzuki, H., et al. 2025, arXiv e-prints, arXiv:2511.14126, doi: [10.48550/arXiv.2511.14126](https://doi.org/10.48550/arXiv.2511.14126)
- Li, Y., Liu, S., & He, Y. 2023, *ApJ*, 953, 100, doi: [10.3847/1538-4357/ace344](https://doi.org/10.3847/1538-4357/ace344)
- Ma, X.-H., Bi, Y.-J., Cao, Z., et al. 2022, *Chinese Physics C*, 46, 030001, doi: [10.1088/1674-1137/ac3fa6](https://doi.org/10.1088/1674-1137/ac3fa6)
- Manchester, R. N., Hobbs, G. B., Teoh, A., & Hobbs, M. 2005, *AJ*, 129, 1993, doi: [10.1086/428488](https://doi.org/10.1086/428488)
- Mattox, J. R., Bertsch, D. L., Chiang, J., et al. 1996, *ApJ*, 461, 396, doi: [10.1086/177068](https://doi.org/10.1086/177068)
- Mizuno, T., Hayashi, K., Ochi, H., et al. 2025, *PASJ*, 77, 965, doi: [10.1093/pasj/psaf069](https://doi.org/10.1093/pasj/psaf069)
- Morris, D. J., Hobbs, G., Lyne, A. G., et al. 2002, *MNRAS*, 335, 275, doi: [10.1046/j.1365-8711.2002.05551.x](https://doi.org/10.1046/j.1365-8711.2002.05551.x)
- Murase, T., Sano, H., Matsubara, K., et al. 2026, arXiv e-prints, arXiv:2601.18040, doi: [10.48550/arXiv.2601.18040](https://doi.org/10.48550/arXiv.2601.18040)
- Ohira, Y., Yamazaki, R., Kawanaka, N., & Ioka, K. 2012, *Monthly Notices of the Royal Astronomical Society*, 427, 91, doi: [10.1111/j.1365-2966.2012.21908.x](https://doi.org/10.1111/j.1365-2966.2012.21908.x)
- Oka, T., Ishizaki, W., Mori, M., et al. 2025, *ApJ*, 989, 137, doi: [10.3847/1538-4357/ade80](https://doi.org/10.3847/1538-4357/ade80)
- Porter, T. A., Jóhannesson, G., & Moskalenko, I. V. 2017, *ApJ*, 846, 67, doi: [10.3847/1538-4357/aa844d](https://doi.org/10.3847/1538-4357/aa844d)
- Ranasinghe, S., & Leahy, D. 2023, *ApJS*, 265, 53, doi: [10.3847/1538-4365/acc1de](https://doi.org/10.3847/1538-4365/acc1de)
- Reich, W., & Sun, X.-H. 2019, *Research in Astronomy and Astrophysics*, 19, 045, doi: [10.1088/1674-4527/19/3/45](https://doi.org/10.1088/1674-4527/19/3/45)
- Sano, H., Yoshiike, S., Yamane, Y., et al. 2018, in *Astronomical Society of Japan Annual Meeting (2018 Spring) Abstract book*, Q15a
- Sawada, T., Ikeda, N., Sunada, K., et al. 2008, *PASJ*, 60, 445, doi: [10.1093/pasj/60.3.445](https://doi.org/10.1093/pasj/60.3.445)
- Seta, A., & McClure-Griffiths, N. M. 2025, *MNRAS*, 539, 1024, doi: [10.1093/mnras/staf520](https://doi.org/10.1093/mnras/staf520)
- Stil, J. M., Taylor, A. R., Dickey, J. M., et al. 2006, *AJ*, 132, 1158, doi: [10.1086/505940](https://doi.org/10.1086/505940)
- Su, Y., Zhou, X., Yang, J., et al. 2017, *ApJ*, 845, 48, doi: [10.3847/1538-4357/aa7f2a](https://doi.org/10.3847/1538-4357/aa7f2a)
- Sun, X.-N., Yang, R.-Z., & Liang, E.-W. 2022, *A&A*, 659, A83, doi: [10.1051/0004-6361/202142394](https://doi.org/10.1051/0004-6361/202142394)
- Suzuki, H., Bamba, A., Enokiya, R., et al. 2020, *ApJ*, 893, 147, doi: [10.3847/1538-4357/ab80ba](https://doi.org/10.3847/1538-4357/ab80ba)
- Suzuki, H., Bamba, A., Yamazaki, R., & Ohira, Y. 2022, *ApJ*, 924, 45, doi: [10.3847/1538-4357/ac33b5](https://doi.org/10.3847/1538-4357/ac33b5)
- Suzuki, H., Plucinsky, P. P., Gaetz, T. J., & Bamba, A. 2021, *A&A*, 655, A116, doi: [10.1051/0004-6361/202141458](https://doi.org/10.1051/0004-6361/202141458)
- Suzuki, H., Tsuji, N., Kanemaru, Y., et al. 2025, *ApJL*, 978, L20, doi: [10.3847/2041-8213/ad9d11](https://doi.org/10.3847/2041-8213/ad9d11)
- Temim, T., Slane, P., Castro, D., et al. 2013, *ApJ*, 768, 61, doi: [10.1088/0004-637X/768/1/61](https://doi.org/10.1088/0004-637X/768/1/61)
- Temim, T., Slane, P., Kolb, C., et al. 2015, *ApJ*, 808, 100, doi: [10.1088/0004-637X/808/1/100](https://doi.org/10.1088/0004-637X/808/1/100)
- The LHAASO Collaboration. 2026, arXiv e-prints, arXiv:2603.15537, doi: [10.48550/arXiv.2603.15537](https://doi.org/10.48550/arXiv.2603.15537)
- Tibet AS $\gamma$  Collaboration, Amenomori, M., Bao, Y. W., et al. 2021, *Nature Astronomy*, 5, 460, doi: [10.1038/s41550-020-01294-9](https://doi.org/10.1038/s41550-020-01294-9)
- Uchiyama, H., Nobukawa, M., Tsuru, T. G., & Koyama, K. 2013, *PASJ*, 65, 19, doi: [10.1093/pasj/65.1.19](https://doi.org/10.1093/pasj/65.1.19)
- Umemoto, T., Minamidani, T., Kuno, N., et al. 2017, *PASJ*, 69, 78, doi: [10.1093/pasj/psx061](https://doi.org/10.1093/pasj/psx061)
- Virtanen, P., Gommers, R., Oliphant, T. E., et al. 2020, *Nature Methods*, 17, 261, doi: [10.1038/s41592-019-0686-2](https://doi.org/10.1038/s41592-019-0686-2)
- Wood, M., Caputo, R., Charles, E., et al. 2017, in *International Cosmic Ray Conference*, Vol. 301, 35th International Cosmic Ray Conference (ICRC2017), 824, doi: [10.22323/1.301.0824](https://doi.org/10.22323/1.301.0824)
- Zabalza, V. 2015, in *International Cosmic Ray Conference*, Vol. 34, 34th International Cosmic Ray Conference (ICRC2015), 922, doi: [10.22323/1.236.0922](https://doi.org/10.22323/1.236.0922)
- Zeng, H., Xin, Y., Zhang, S., & Liu, S. 2021, *ApJ*, 910, 78, doi: [10.3847/1538-4357/abe37e](https://doi.org/10.3847/1538-4357/abe37e)
- Zhang, H.-M., Xi, S.-Q., Liu, R.-Y., et al. 2020, *ApJ*, 889, 12, doi: [10.3847/1538-4357/ab5af6](https://doi.org/10.3847/1538-4357/ab5af6)